

# Real space tests of the statistical isotropy and Gaussianity of the WMAP CMB data

Bartosz Lew<sup>1,2,3,\*</sup>

<sup>1</sup>*National Astronomical Observatory, 2-21-1 Osawa, Mitaka, Tokyo 181-8588, Japan*

<sup>2</sup>*Department of Physics and Astrophysics, Nagoya University, Nagoya 464-8602, Japan*

<sup>3</sup>*Toruń Centre for Astronomy, Nicolaus Copernicus University, ul. Gagarina 11, 87-100 Toruń, Poland*  
(Accepted 09 July 2008)

We introduce and analyze a method for testing statistical isotropy and Gaussianity and apply it to the Wilkinson Microwave Anisotropy Probe (WMAP) cosmic microwave background (CMB) foreground reduced, temperature maps. We also test cross-channel difference maps to constrain levels of residual foregrounds contamination and systematical uncertainties. We divide the sky into regions of varying size and shape and measure the first four moments of the one-point distribution within these regions, and using their simulated spatial distributions we test the statistical isotropy and Gaussianity hypotheses. By randomly varying orientations of these regions, we sample the underlying CMB field in a new manner, that offers a richer exploration of the data content, and avoids possible biasing due to a single choice of sky division. In our analysis we account for all two-point correlations between different regions and also show the impact on the results when these correlations are neglected. The statistical significance is assessed via comparison with realistic Monte-Carlo simulations.

We find the three-year WMAP maps to agree well with the isotropic, Gaussian random field simulations as probed by regions corresponding to the angular scales ranging from  $6^\circ$  to  $30^\circ$  at 68% confidence level.

We report a strong, anomalous (99.8% CL) dipole “excess” in the V band of the three-year WMAP data and also in the V band of the WMAP five-year data (99.3% CL).

Using our statistic, we notice the large scale hemispherical power asymmetry, and find that it is not highly statistically significant in the WMAP three-year data ( $\lesssim 97\%$ ) at scales  $\ell \leq 40$ . The significance is even smaller if multipoles up to  $\ell = 1024$  are considered ( $\sim 90\%$  CL). We give constraints on the amplitude of the previously-proposed CMB dipole modulation field parameter.

We find some hints of foreground contamination in the form of a locally strong, anomalous kurtosis-excess in the Q+V+W co-added map, which however is not significant globally.

We easily detect the residual foregrounds in cross-band difference maps at rms level  $\lesssim 7\mu\text{K}$  (at scales  $\gtrsim 6^\circ$ ) and limit the systematical uncertainties to  $\lesssim 1.7\mu\text{K}$  (at scales  $\gtrsim 30^\circ$ ).

## I. INTRODUCTION

Observational cosmology has established the flat  $\Lambda\text{CDM}$  model with nearly scale invariant initial density perturbations as the standard model of modern cosmology (e.g. Astier et al. (2006); Cole et al. (2005); Eisenstein et al. (2005); Hinshaw et al. (2007); Page et al. (2007); Riess et al. (2004); Spergel et al. (2007); Tegmark et al. (2006)). These observations seem consistent with the simplest predictions from inflation theory. Amongst those predictions, one consequence from the cosmological principle, the statistical isotropy (SI), and one generic consequence from inflation theories, the Gaussianity (to leading order) of the cosmic microwave background (CMB) temperature fluctuations, have received a lot of attention with the release of the first year of observations of the WMAP satellite. The relevant statistical analyses either aimed at detecting small amounts of non-Gaussianity (NG), that stems from non-linear effect even within inflation theories (Bartolo et al. 2004), or looked for any anomalous signal that would challenge this standard model.

However, separating SI from Gaussianity is a delicate task when making such a test, since one has to deal with only one realization of the CMB, that is considered in this context to be a random field. SI and NG have been tested in variety of ways and some “anomalies” have been reported. In particular, using tests optimized for SI, in spherical harmonic (SH) phase space (de Oliveira-Costa et al. 1996, 2004) an unusual alignment (98% CL) at low multipoles have been found and confirmed (e.g. Copi et al. (2006);

Land & Magueijo (2005a)). Number of other tests and statistical tools and estimators have been devised and used to constrain SI and/or NG. Among others, these include: bipolar power spectrum (Hajian & Souradeep 2006), phase correlations tests (Naselsky et al. 2005), higher order correlations in SH space (bi/tri-spectrum) e.g. (Cabella et al. 2006, 2005; Ferreira et al. 1998; Magueijo & Medeiros 2004),  $n$ -point real space statistics: (Durrer et al. 2000; Gaztañaga & Wagg 2003; Gaztañaga et al. 2003), morphological estimators (like Minkowski functionals) (Park 2004; Shandarin 2002; Wu et al. 2001), multipole vectors (Copi et al. 2006, 2004; Land & Magueijo 2005b; Schwarz et al. 2004) higher order correlation functions (Gaztañaga & Wagg 2003), phase space statistics (Chiang et al. 2003; Naselsky et al. 2005), wavelet space statistics (Cruz et al. 2007; McEwen et al. 2006a,b; Vielva et al. 2004), higher criticism statistic (Cayón et al. 2005), pair angular separation histograms (Bernui et al. 2007) and also various real-space based tests eg: Eriksen et al. (2007, 2004); Hansen et al. (2004a,b) In particular a dedicated tests of hemispherical power asymmetry have been reported by many authors and found anomalous at confidence levels ranging from  $\sim 2\sigma$  to  $\sim 2.6\sigma$  (95%CL  $\sim$  99% CL)

In this work, we measure regional one-point statistics in the WMAP data and in simulations in order to test the SI and Gaussianity hypotheses. We mean to extend and generalize the previous similar works in three ways.

Firstly, we show that the result of the analysis strongly depends on the way in which the sky is partitioned into regions for the subsequent statistics, and we circumvent this problem by relaxing the constraints on the shape and the orientation of a chosen sky pixelization by considering many randomly oriented sky regionalizations. This allows us to avoid a possible bias in such regionalization analysis that is constrained only to a single choice of pixelization scheme.

Secondly, we relax the constraint on the size of the re-

\*blew@a.phys.nagoya-u.ac.jp

gions, thereby statistically probing features at different angular scales.

Thirdly, we account for all correlations between different regions, resulting from the well known two-point correlations (or possible higher-order correlations) using multivariate full covariance matrix calculus for more robust estimation of the statistical significance of local departures from Gaussian random field (GRF) simulations.

We will assess the statistical significance of our results in three different manners so as to avoid the standard pitfalls of such an analysis and will rely heavily on realistic simulations to either probe the underlying distributions or to test the sensitivity of our statistic.

The paper is organized as follows: in Sect. II we introduce the data sets that are being tested, and provide details of the simulations. In Sect. III we describe the details of our statistical approach for regional statistics. We then test and illustrate the sensitivity of our statistics via Gaussian and non-Gaussian simulations in Sect. IV before presenting the results in Sect. V and discussing them in Sect. VI. We conclude in Sect. VII.

## II. DATA AND SIMULATIONS

For the main analysis in the paper we use the WMAP three-year foreground reduced temperature maps from differential assemblies (DA) Q1, Q2, V1, V2, and W1, W2, W3, W4, pixelized in the *HEALPIX* sphere pixelization scheme with resolution parameter  $N_s = 512$ . We co-add them using inverse noise pixel weighting (Eq. 1) and form either individual frequency combined maps (Q, V, W) or an overall combined map (Q+V+W) to increase the signal to noise ratio according to:

$$T_i = \frac{1}{W_i} \sum_{j=j_{st}}^{j_{en}} w_{ji} T_{ji} \quad (1)$$

where  $W_i = \sum_{j=j_{st}}^{j_{en}} w_{ji}$  and  $w_{ji} = N_{ji}/\sigma_{0j}^2$  and  $\sigma_0$  is the noise rms for a given DA and  $N_{ij}$  is the number of observations for the  $i$ th pixel for  $j$ th DA (Hinshaw et al. 2007). The sum over  $j$  iterates the DAs whose maps are co-added (in numbers, {2, 2, 4, 8} respectively for Q, V, W and all channels). We will refer to those datasets as Q, V, W and INC (inverse noise co-added map) respectively and define a data set vector  $d \in \{Q, V, W, INC\}$  for further reference.

We also consider a difference maps between different channels to independently test the residual foregrounds and to cross-check with the results obtained from the single band NG analysis. We consider a single band difference maps (e.g. Q1-Q2, V1-V2) as well, since nearly identical frequency difference maps have a negligible amount of CMB or foreground signal<sup>1</sup> and these are used to test the consistency of our white noise realizations against the pre-whitened  $1/f$  pink noise of the WMAP data and constrain the systematical uncertainties.

<sup>1</sup> The non-vanishing CMB or foregrounds content, even in the single band differential maps, comes from slight differences in the effective working frequencies of the differential assemblies (DAs) and also from slightly different beam profiles. While in case of the single band difference maps (e.g. Q1-Q2) the residual rms signal is weaker than the noise by more than two orders of magnitude, in case of the different frequency bands (e.g. Q-V) the residual CMB rms signal is about one order of magnitude weaker than the noise.

Details of this check is given in appendix C. We will refer to these maps as QV, QW or VW for cross-band difference maps and Q12, V12 etc. for an individual differential assembly difference maps.

As an extension to the main analysis we also test the five-year WMAP data set from the V channel and refer to it as V5. For this purpose the WMAP five-year simulations are used and preprocessed in the same way as in case of the WMAP three-year data except for the sky-mask, which here we choose to be KQ75.

The residual monopole, measured outside the three-year release of the Kp0 (hereafter the Kp03) sky mask, is removed from each map by temperature shift in real space. The Kp03 sky mask (including galactic region and bright point sources) is applied and no downgrading is performed at this level. We will use  $N_{sim} = 10^4$ , realistic, full resolution simulations to test our statistics and to assess confidence thresholds (see Appendix A for details and basic tests).

## III. DIRECTIONAL STATISTICS

If the CMB sky is a realization of a multivariate Gaussian random field (GRF), then statistics of any linear statistical estimator should not deviate from Gaussianity within any arbitrary region in the sky. Otherwise - in case of non-linear estimators - in general deviations from Gaussian statistics are expected, hence MC approach for assessing limits on consistency with Gaussianity is used.

In order to test the *stationarity* and Gaussianity of the temperature fluctuation hypotheses we use two independent sphere pixelization schemes to define sky divisions and consequently a set of adjacent, continuous regions.

### A. Sky pixelizations

The first pixelization scheme (hereafter referred to as *HP*) is an independent implementation of the *HEALPIX* pixelization scheme (Górski et al. 2005) and its resolution is parametrized by the  $n_s$  parameter (Fig. 1 top-left). The total number of pixels for a given  $n_s$  is  $r = 12n_s^2$ . We will use three different resolutions ( $n_s$ ) as specified in Table I.

The second one (hereafter called *LB*) covers the sphere by dividing it along lines of parallels (iso-latitude) and meridians (iso-longitude) to obtain arbitrarily elongated pixels, generally of varying angular sizes (Fig. 1 top-right). This results in the total number of pixels  $r = N_l N_b$  (where  $N_l$  and  $N_b$  are the numbers of longitudinal and latitudinal divisions). The three different resolutions used in the analysis defined by these parameters are specified in Table I. Further flexibility is allowed by rotating the polar axis by three randomly chosen Euler angles.

Since there is no reasonable, physical motivation for preferring any particular sky pixelization over another from the standpoint of testing a GRF hypothesis, we consider  $N_m = 100$  random orientations for each of the six types of pixelization schemes, which altogether yields 600 different sky pixelizations with a total number of 280 000 regions of different shapes and sizes probing different angular scales (Fig. 2). We therefore draw the three Euler angles used to define the axis position and pixelization scheme orientation about this axis from a uniform distribution.

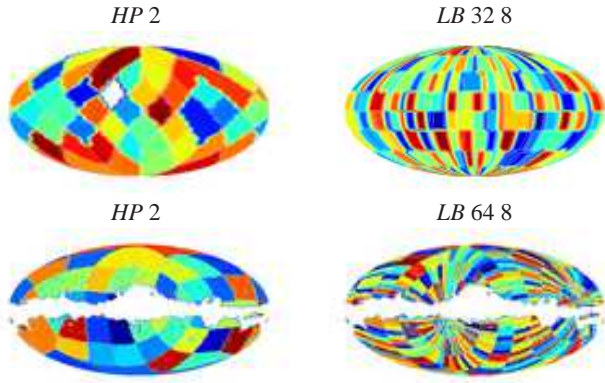


Fig 1: In the first row, two lowest-resolution pixelization schemes – *HP 2* (top-left) and *LB 32 8* (top-right) are shown. In the second row, we present an examples of two *multi-masks* actually used in analysis. Pixelization schemes are rotated to a random orientation, with Kp03 sky mask applied. These are *HP 2* (lower-left) and *LB 64 8* (lower-right) respectively. Values in all regions were randomized for better visualization.

All sky pixelizations are subject to the Kp03 (three-year Kp0) galactic/point sources cut which masks  $\sim 23\%$  of the sky. In practice there is no lower bound for the size of a region due to its random orientation with respect to the Kp03 sky cut. However for the sake of numerical stability, when computing the inverse covariance matrix (see below), we only consider regions that happen to have  $N_{pix} > N_{pixth} = 100$ , where  $N_{pix}$  refers to the number of pixels of the original  $n_s = 512$  map falling into this particular region.

Hereafter we refer to a particular random realization of a pixelization scheme (a random set of regions covering the full sky and merged with Kp03 sky mask) as a *multi-mask*, since it uniquely tags sky regions and allows to pursue statistics exclusively within them (see Fig. 1 bottom-left and bottom-right). Of course different *multi-masks*, even defined from a similar pixelization scheme, may have a different number of regions due to the random orientations with respect to the Kp03 sky mask. We define  $N_{reg}(r, m)$  as the number of regions of a *multi-mask* as a function of initial resolution parameter  $r$  and *multi-mask* ID number  $m \in \{1..N_m\}$ . As an illustration, the two lowest resolution, pixelization schemes and two examples of *multi-masks* are shown in Fig. 1. We will also use additional sets of *multi-masks* to complete and extend the main part of the analysis in a few selected cases.

## B. One-point statistics

In each of the defined regions of each *multi-mask*, the first four central moments (i.e. mean ( $m$ ), standard deviation ( $\sigma$ ),

Table I: Summary on the *LB* and *HP* pixelization schemes and resolutions used in the main analysis, given explicitly for quick reference. The columns abbreviations are as follows: (1) pixelization scheme reference name, (2) resolution parameter value, (3) approximated angular size of regions, (4) number of regions in pixelization scheme.

HP				LB				
(1)	(2)	(3)	(4)	(1)	(1)	(3)	(4)	
Ref. name	Res. $n_s$	Ang.size $\Omega_{reg}$ [deg]	regs. $r$	Ref. name	Res. $N_l$	Ang.size $\Delta_l$ [deg]	regs. $N_b$	
<i>HP 2</i>	2	29.3	48	<i>LB 32 8</i>	32	8	11.3	22.5
<i>HP 4</i>	4	14.6	192	<i>LB 64 8</i>	64	8	5.6	22.5
<i>HP 8</i>	8	7.3	768	<i>LB 64 16</i>	64	16	5.6	11.3

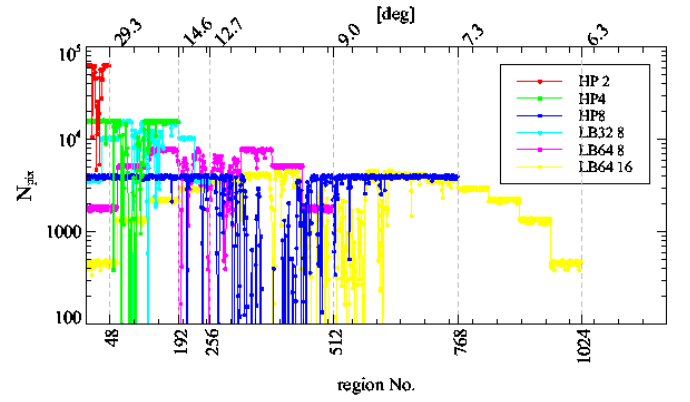


Fig 2: Number of points,  $N_{pix}(k)$ , in regions for all 6 types of pixelization schemes used in their initial position, after masking by Kp03 sky mask, in function of region number. All regions with  $N_{pix} < 100$  were not considered in the analysis as detailed in the text and treated as masked. The central parts ( $\sim r/2$ ) of a given pixelization are strongly covered by the Kp03 mask (this is true only for the particular initial orientation of a *multi-mask*). At the top abscissa we give the approximate angular scales probed by pixelization schemes with the corresponding total number of regions indicated in the bottom abscissa.

skewness (S), and kurtosis (K)), of the underlying temperature fluctuations are computed for the data and for all  $N_{sim} = 10^4$  simulations. Together this yields  $2.8 \times 10^9$  regions for assessment of uncertainties. As will be shown in the Sect. IV, allowing for arbitrary orientations of *multi-masks* has an impact on the results and yield a more stringent test on stationarity. The fact that we choose to work in real space allows for a good localization of deviations in the sky.

The presence of extended, residual foregrounds or unresolved, unresolved point sources, will affect the local central moments distributions. In particular the mean of the fluctuations will tend to be up-shifted with respect to simulations if diffuse foregrounds are present or down-shifted if they are over-subtracted. Also, depending on the amplitude of the residual foregrounds the local variance will also be altered. Looking jointly at the distribution of these moments on large scales might also provide a handle on the large scale distribution of power via the off-diagonal terms of the inverse covariance matrix. The physical extent and position of the regions where particular type of deviation occurred can provide a clue to the possible nature of the foregrounds causing it (see Sect. IV).

## C. Assessing statistical significance

Since our measurements are statistical, a crucial stage remains in probing their statistical significance. Our approach relies on a detailed comparison between the measurements performed on real data with the distribution of the same measurements performed on simulations.

We consider three different ways to address the significance of these measurements. Each step involves one extra-level of generality and will shed light on the subtleties of such an assessment.

At first, we look at individual regions, ignore their correlations and compare them with the simulations. We call this approach the “individual region analysis”. It is the simplest

approach one can consider.

Secondly, we compute the overall statistical significance per *multi-mask*, by taking into account the two-point correlations between moments of distributions (MODs) measured in regions of the same *multi-mask* via the full covariance matrix. We call this approach the “multi-region analysis”. The resulting probabilities  $P(\chi_q^2)$  (Eq. B7) are the joint probabilities of exceeding a certain confidence threshold as a function of pixelization scheme ( $r$ ), *multi-mask* ( $m \in \{1..N_m\}$ ), MOD ( $X \in \{m, \sigma, S, K\}$ ), and dataset ( $d \in \{Q, V, W, INC\}$ ) configured by a parameter vector  $\mathbf{q} = \{X, r, m, d\}$ . This analysis extends the information from the single region analysis by testing the consistency of the data with the simulations via standard multivariate calculus.

Finally, we combine all the information probed by different *multi-masks* to find the joint cumulative probability of rejecting the GRF hypothesis as a function of pixelization scheme ( $r$ ), MOD ( $X$ ), and dataset (eg. frequency) ( $d$ ). We call this approach the “all *multi-masks* analysis”.

We remind that the statistical significance of any real data measurement, at any stage of the analysis, is always assessed by a comparison to the set of the same measurements performed using GRF simulations. The exact details of the analysis at each step are given in Appendix B.

#### D. Visualizing the results

To visualize our results from the single-region analysis, or multi-region analysis at certain confidence level, we proceed the following way. For individual region statistics, for each region of each *multi-mask* we define  $n_\sigma$  as

$$n_\sigma = \sqrt{2}\text{erf}^{-1}(1 - P(X)) = \text{cdf}_G^{-1}(P(X)/2) \quad (2)$$

where  $P(X)$  is the quantile probability derived according to Eqs. B3 and B4. The  $n_\sigma$  thus defined is the Gaussian number of  $\sigma$ s by which a region, defined by a given *multi-mask*, deviates from simulation average. We then produce maps of  $n_\sigma$  estimator, for data processed through each of the 600 generated *multi-masks* and for each MOD. Then, to present all the results in a compact way, we scramble these maps within the same MOD. We over-plot the individual pixels from regions with the strongest deviations from the underlying pixels. Positive  $n_\sigma$  values correspond to excessive value of a given MOD in a region, and negative value correspond to its suppression. For clarity, we use a threshold  $|n_{\sigma,th}| = 3$  to produce maps with only the strongest ( $3\sigma$ ) detections.

For the joint multi-region statistics we produce maps (as detailed above) using only those *multi-masks* that yield  $|P(\chi_q^2)| \leq P_{th}$  (Eqs. B3, B4) revealing detections at the statistical significance  $1 - P_{th}$  for a given MOD, *multi-mask* resolution  $r$  and dataset  $d$ , i.e. for a given parameter  $\mathbf{q}$ . Within this notation, single region statistics corresponds to  $P_{th} = 1$ .

While the “n-sigma” maps are easy to read when looking at distributions of the anomalies at a given local significance, they are unitless and cannot be directly linked with quantities that are physically measured. We therefore also consider a difference maps ( $\Delta$  maps<sup>2</sup>) of regional departures in indi-

vidual MODs between datasets and averaged simulation expectation: i.e. for  $i$ th region of a given *multi-mask* we plot  $\Delta_i = X_i - \langle X_i \rangle_N$ , where  $\langle \rangle_N$  stands for average over  $N$  simulations.

## IV. TESTS OF THE SIMULATION AND MEASUREMENT PIPELINE

In order to validate the statistical tools introduced above, test the sensitivity and the correctness of the numerical code, we performed a set of experiments using both simulated WMAP CMB data and data with either simulated violation of the large scale statistical isotropy or localized NG features.

### A. Consistency check with GRF simulations

We first test self-consistency by generating 10 additional INC CMB data sets and carry out for each of them the single-region, joint multi-region and all *multi-masks* statistics. As expected, we found that the simulated datasets yield a good consistency with the simulations (at 68% CL).

### B. Sensitivity to local NG

For a statistically isotropic Gaussian process the kurtosis is expected to be exactly equal to  $K = 3$ , which translates into a kurtosis excess  $\text{KE} = K - 3 = 0$ . Violation of either of the assumptions can lead to a positive or negative KE.

At first we simulate what could be a residual component, resulting from subtraction of a non-ideal foreground template, extended over an area of  $10^\circ$  angular, centered at  $(l, b) = (50^\circ, 50^\circ)$ , whose signature would be a non-vanishing KE. Such residuals must be expected to be small in the foreground-cleaned maps, and they could be either positive – resulting from foregrounds undersubtraction – or negative ones – resulting from foregrounds oversubtraction.

Therefore, the introduced NG component is drawn from a normal distribution with variance  $\sigma^2$  and with a mean increasing uniformly across the patch when going north-south following Healpix ring ordering inside the spot. From the northern point of the patch down to the southern part of the patch, the mean will shift by  $2n\sigma_{\text{CMB}}$ .

We introduce in this way a gradient in the noise and thus a non-zero local negative KE (Fig. 4) but still preserve a vanishing (within the spot) skewness. The  $\sigma$  value is chosen to be 1% of the underlying CMB rms ( $\sigma_{\text{CMB}}$ ). To test the sensitivity of our estimator we consider  $n$  to be either 1 or 2, above which the NG template starts to be visually noticeable due to edge discontinuities. Note that, with a so defined anomaly, the pixels of the spot that are close to its horizontal diameter will have the least impact on the underlying CMB field distortions.

The choice of the  $n$  parameter values corresponds to the NG signals of the rms amplitude  $\sim 50\mu\text{K}$  and  $\sim 100\mu\text{K}$  for  $n = 1$  and 2 respectively within the spot. We note that the rms. value within the spot of the same size, in the foregrounds reduced difference VW map of the WMAP3 data, yields  $> 100\mu\text{K}$  depending on the exact location of the spot in the sky, hence our choice of NG signals amplitude aim at detection of relatively small anomalies as compared to the WMAP3 noise specifications.

<sup>2</sup> We will hereafter refer to maps so produced as  $\Delta$  maps to make a clear distinction from the difference maps obtained by differentiation of temperature maps from different frequencies (e.g. QV, QW, etc...)

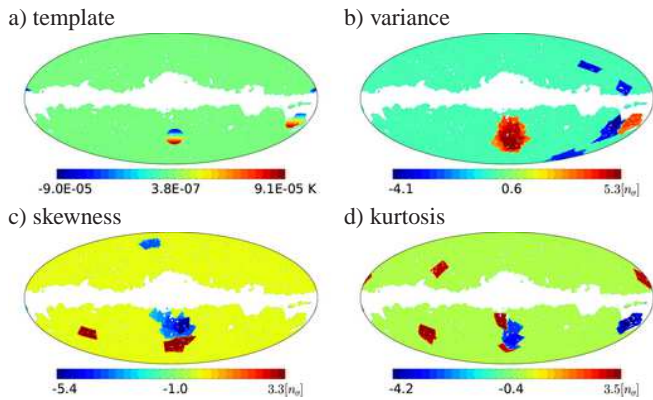


Fig 3: *a)* A Non-Gaussian temperature gradient template, leading to locally negative kurtosis excess. The parameter value of  $n = 2$  is used (see the main text for details). Note that one of the spots is practically removed by the galactic sky cut. *b-d)* The results of the single-region analysis using the 100 *multi-masks* of the *HP* 4 pixelization scheme of one of the simulated INC data and contaminated with the template. The scrambled  $n_\sigma$  detection map in variance, skewness and kurtosis, thresholded at  $n_{\sigma,th} = 3$ , is plotted. Note the strong, template-induced, local anomalies detections traced by different *multi-masks*, as well as some other, but somewhat weaker, detections of  $|n_\sigma| > 3$  regions. In particular, the template leads to the local kurtosis suppression and strong local excess of the variance.

We find that for a single NG spot of radius  $10^\circ$ , the multi-region analysis does not return any significant detection for  $n = 1$  in any of the MODs, but the single region analysis finds the contaminated regions unusual at  $n_\sigma \approx 2.5$ . In case of  $n = 2$  we detected a  $3\sigma$  local deviation in kurtosis, while in all-*multi-masks* analysis we reject Gaussianity at 99.8% CL (*HP* 8) due to variance distributions<sup>3</sup>.

We rerun the test for the same type of NG templates but replicated in 3 disjoint spots at different directions in the sky for the same values of  $n$  parameter (Fig. 3-a).

The choice of the position and the size of the spots is most relevant to the results presented in Section V. The results of the single region analysis is shown in Fig. 3(b)-(d). Note how different *multi-masks* trace the locally introduced anomaly. Depending on the orientation of the *multi-mask* and its regions around the directions of the NG spots, the returned  $n_\sigma$  values differ. In the overall multi-region analysis this naturally leads to a distribution of probabilities which strongly depend on how the features of the map are split and probed by different regions.

Note that some of the *multi-masks* also return an  $n_\sigma > 3$  detections even in a template-free regions. It is therefore clear that use of many differently oriented *multi-masks* helps to investigate the statistical significance of local anomalies.

The multi-region analysis in case of  $n = 1$  return no significant detections in any of the MODs, but very significant deviations were detected for the case  $n = 2$  in all-*multi-masks* analysis (Table II in section "KE-"), again only in the variance distributions.

Consequently, we find that for the unfiltered maps the distributions of variances are actually more sensitive to this kind of simulated anomalies, rather than higher order MODs. We

note, however, that measuring a local sign of KE may be a hint of the nature of the foregrounds signals as the kind of template used in this example introduces locally only the negative KE as shown in Fig. 4. Similar dependences are obtained for tem-

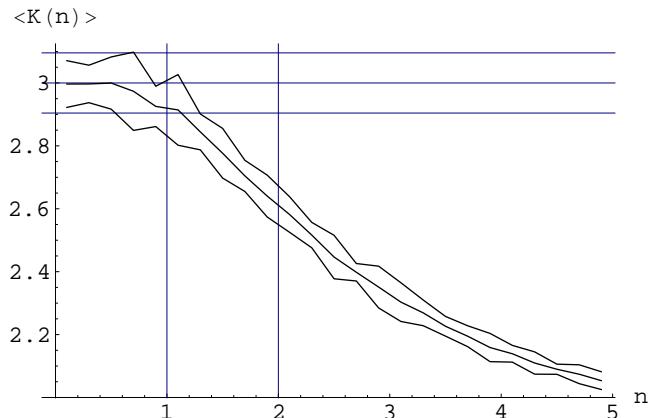


Fig 4: Negative departure of the kurtosis in the NG spot as a function of  $n$  parameter. The plot shows the kurtosis of a sum of GRF and the generated NG template averaged over 10 random realizations of the two. The variance of the GRF is 100 larger than the variance of the NG template and the field size is chosen to correspond to the NG spot size as described in the text. The  $3\sigma$  confidence thresholds were quoted around the expected values for the GRF only and for the GRF+NG template cases. Vertical lines indicate the chosen values of the  $n$  parameter used for the templated maps generation for the test.

plates of different shapes and sizes and combinations of these factors. In the limit of a flat template ( $n = 0$ ) the field becomes Gaussian, as expected.

It is possible to introduce a non-vanishing skewness by making the template unsymmetrical, by considering shifts in the mean which are unsymmetrical about zero. A similar effect is possible by considering regions of *multi-masks* that only partially overlap with the area of the NG spot (Fig. 3c). Note that the example from Fig. 4 does not include the effects of the non-uniform noise component which is included in our tests and also that the confidence level contours were derived assuming the Gaussian error statistics; therefore it is not straightforward to extrapolate the strong detections expected from Fig. 4 for  $n = 2$  onto the full sky, locally templated, signal and noise realizations, subject to subsequent regional statistics.

Note that the assumed size of local deviations is small relative to the full sky one, and hence their global impact is reduced accordingly. Larger, in sense of area, deviations will be of course easier to detect. Also a specific pre-filtering in the spherical harmonic (SH) space, of the data prior to the test may help to expose the most relevant scales to the test. In this test we focused on testing unfiltered maps; therefore, necessarily the strength of the detections must be suppressed.

It is not possible to obtain a locally positive KE with the above-described template. Such deviation could however be the signature of the unresolved point source contribution<sup>4</sup>, or an unknown and localized noise contribution.

Again, for qualitative studies only, we simulate the point source component in the full sky by adding random num-

<sup>3</sup> Of course, the estimated rejection confidence thresholds given in Table. II based only on a single-simulation measurements may be somewhat biased depending on particular realization of the GRF simulation.

<sup>4</sup> Although this would have a specific frequency dependence, we ignore this fact here.

bers drawn from a distribution which is an absolute value of the Gaussian distribution with zero mean and random variance  $n\sigma_{\text{CMB}}$  parametrized by parameter  $n$  and uniformly distributed within range  $[0, n\sigma_{\text{CMB}}]$ , where  $\sigma_{\text{CMB}}$  is the rms value of the underlying CMB fluctuations.

From our simulations however, it appears that it is difficult to detect a significant contribution due to point source contamination since such signal is significantly smeared by the instrumental beam even for  $n$  as large as 6. Even when  $\text{KE} \gtrsim 6$  before beam smearing, the variance response is much stronger than the KE response leading to inconsistencies with simulations in the total power of the map as measured by e.g. full sky variance distribution (Fig. 18). We therefore conclude that it is unlikely to detect any point source contribution to KE in this test which is not surprising since we work at fairly low resolution which dilutes the point source signal.

As already mentioned, a locally generated noise-like component in the map, in principle, could generate a non-negligible positive  $\text{KE}^5$  as it would not be processed by the instrumental beams. However since such noise is not well motivated physically due to non-local properties of the TOD data and scanning strategy of the WMAP, and also since the noise properties are well constrained, therefore we do not consider such case.

We conclude that small and single (compared to full sky observations) localized NG features will be difficult to detect via higher order MODs in the joint multi-region and all-*multi-masks* analysis due to their small statistical impact on the overall statistics. However a single region statistics carried out first might be a rough guide in selecting a possibly interesting foreground NG signals. If these indicate regions with significant deviations in variance and possessing a negative KE it would hint on residual, large scale foreground contamination.

### 1. Stability of results in function number of multi-masks

As different *multi-masks* probe the underlying data differently, the joint-probabilities per *multi-mask* differ and lead to a distribution that typically covers a wide range of possible probability values. As such, the multi-region analysis (see sec. B 2 for details) can be used to find the orientation of the most unusual regions in the *multi-masks* that yield the smallest probability as compared to GRF simulations.

Since from the point of view of statistical isotropy all *multi-masks* are equivalent, in the all-*multi-masks* analysis (see sec. B 3 for details) we integrate the information from all *multi-masks* within a pixelization scheme to obtain an average level of consistency of the data with GRF simulations for that pixelization scheme. This approach also provides a conservative way of averaging over a possibly-spurious detections that could be a fluke, due to some accidental arrangement between a *multi-masks* and a data set. If the anomalous feature in the map is strong enough to be detected in many *multi-masks* then this will also result in a detection in the joint all-*multi-masks* analysis. Conversely, if only one or few *multi-masks* result in a very small probability the overall impact will not be large due to stability of the median estimator with respect to the distri-

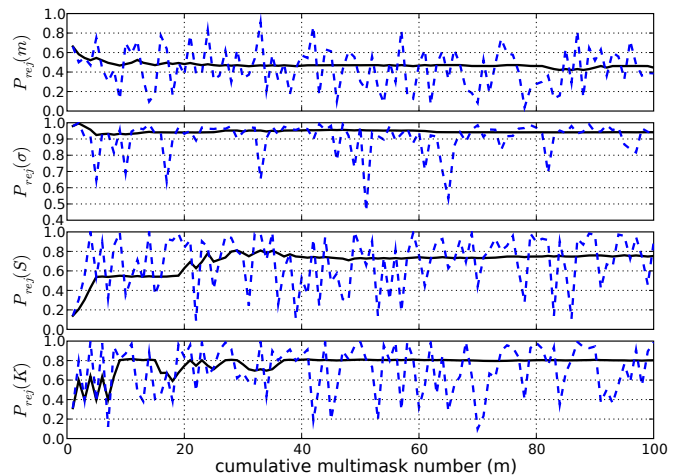


Fig 5: Convergence of the joint all *multi-masks* probability to the value reported in Table II (in section (2KE-) for  $n = 2$ ) for the case of *HP 2* pixelization scheme in function of the cumulative number of *multi-masks* used to derive it (black solid lines) for mean (top panel), variance, skewness and kurtosis (bottom panel). Additionally we overplot the joint multi-region probabilities per *multi-mask* for each *multi-mask* number (blue dashed lines).

bution outliers. However, the investigation of the most anomalous *multi-masks* may help in selecting the deviating regions for further analyses.

In this section we show how the convergence to the results of the all-*multi-masks* analysis is reached in function of number of *multi-masks* used to derive the median  $\chi^2$  value and the corresponding median  $\chi^2$ -distribution leading to the all-*multi-masks* probability. As shown in Fig. 5 the convergence of the joint all-*multi-masks* probability to the reported value for  $N_m = 100$ , is in this case (*HP 2* pixelization scheme) quite fast; however in general it depends on particular properties of the map as well as on the set and ordering of the *multi-masks* used. The speed of the convergence and the robustness of the final value is as good as the convergence of the unbiased mean estimator - i.e. the median - to the intrinsic mean value as the number of random trials (corresponding to the number of *multi-masks*) probing the underlying distribution increases.

Note how strongly the joint probability per *multi-mask* depends on the orientation of the *multi-mask* (blue-dashed lines in Fig. 5). In particular for the variance case, the probabilities of rejection per *multi-mask* range from 45.7% for *multi-mask*  $m = 51$ , to 99.8% for *multi-mask*  $m = 2$ . Yet the, reported in all-*multi-masks* analysis, median value is very stable with respect to these variations.

### 2. The shape of multi-mask regions.

Naturally, the *multi-masks* having large regions will be insensitive to the small scale map features, while the *multi-masks* having small regions will be insensitive to the large scale structures. This motivates the usage different number of regions to probe different scales of the map.

Theoretically there are infinitely many ways of defining the shape of regions of *multi-masks*, and of course, our choice of the shape of pixelization schemes and the *multi-masks* is somewhat arbitrary; however the motivation for using different shapes of regions is straightforward: to probe the data

<sup>5</sup> This is most easily seen in the contribution of the anisotropic noise of the WMAP to the kurtosis of the signal only simulated map, which induces a significant positive overall KE value in the simulation.

using different binning techniques since the GRF statistically should not depend on it. However if the data turns out to be non-random it is possible that the non-randomness will be explored differently by different region shapes. A loose analogy to the real-space *multi-mask* region shape, which is used to derive a local value of an estimator, over the defined area for a given orientation of *multi-mask*, is in the wavelet space the shape of the mother wavelet, which is used to obtain the local convolution coefficients for the input map. In this analogy the size of the region corresponds to the wavelet scale.

### C. Sensitivity to the large scale phase anomalies

We test the sensitivity of our method to the well known large scale anomalies found in the WMAP data: i.e. to the aligned and planar low multipoles  $\ell = 2$  and  $\ell = 3$ . In order to test such anomalies we generate two GRF CMB simulations. In both simulations we use the same realization of the power spectrum and phases as in the case of the first GRF simulation (Sect. IV A).

In the first simulation we enforce large scale phase correlation by introducing an “m-preference” in the power distribution in the quadrupole ( $\ell = 2$ ) and octupole ( $\ell = 3$ ). We choose the “sectoral” spherical harmonic coefficient  $a_{\ell l}$ , to carry all the power of the multipoles. In the second simulation we extend this modification up to  $\ell = 5$ . The GRF signal simulations are rotated to a preferred frame prior the introduction of the planar multipoles. The signal maps are then rotated back to the original orientation so that the maximal momentum axis was located at  $(l, b) = (260^\circ, 60^\circ)$  before adding noise.

As shown in Table II such anomalies have not been significantly detected at tested scales. Although it is expected and observed that considering unfiltered maps (containing all multipoles information mixed together) there will be a little overall impact on the statistics we note a higher sensitivity would be obtained if a prefiltered in SH space data were used.

### D. Sensitivity to the large scale power anomalies

We give a special attention to testing the sensitivity of the method for detecting and quantifying the previously reported large scale anomaly in the power distribution in the sky (Eriksen et al. 2007, 2004). We create a simulated CMB maps where the CMB signal is modulated according to:

$$\begin{aligned} T(\hat{\mathbf{n}}) &= T_{CMB}(\hat{\mathbf{n}})(1 + M(\hat{\mathbf{n}})) \\ M(\hat{\mathbf{n}}) &= A_{\ell_{\max}} \hat{\mathbf{n}} \cdot \hat{\mathbf{d}} \end{aligned} \quad (3)$$

where  $\hat{\mathbf{n}}$  is a unit vector and  $M$  is a bipolar modulation field, oriented in direction  $\hat{\mathbf{d}} = (225^\circ, -27^\circ)$  with amplitude  $A_{\ell_{\max}} \in \{0.114, 0.2\}$  which modulates the CMB component up to the maximal multipole of  $\ell_{\max} = 1024$ .

The result of the test with such modulated simulation is given in Table II (in section “M”). As the amplitude of  $A = 0.114$  has been previously claimed to be preferred for the CMB data (Eriksen et al. 2007) we process five additional, full resolution V simulations, modulated with this amplitude, to reduce a potential biases from a single draw of a random simulation, and report (Table II in section “<M>”) the average rejection thresholds as a function of the pixelization scheme.

Table II: All-*multi-masks* analysis results from tests of the simulated datasets. The columns content is as follows: (1) pixelization scheme, (2..4) “probability of rejecting” the consistency with GRF simulations (Sect. B 3) for each MOD. The abbreviations of the datasets are: 1KE-: INC simulation with one NG spot (three NG spots) leading to  $KE < 0$  and  $n = 1$  (see text Sect. IV for details), 2KE-: INC simulation with one NG spot (three NG spots) leading to  $KE < 0$  and  $n = 2$  (see text Sect. IV for details), A2..3: INC simulation with aligned multipoles  $\ell = 2$  and  $\ell = 3$ , A2..5: INC simulation with aligned multipoles from  $\ell = 2$  to  $\ell = 5$ , M: INC dipole modulated simulation with dipole amplitude of  $A_{\ell_{\max}}$ . <M>: V simulation with CMB signal fully (partially) modulated according to parameter  $A_{\ell_{\max}}$ . The average confidence thresholds are given. The values are rounded to integer percentiles in case of probabilities  $\leq 99\%$  CL. The saturated values are marked with  $\star$ .

Reg.sk.	$P_{rej}^m$ [%]	$P_{rej}^\sigma$ [%]	$P_{rej}^S$ [%]	$P_{rej}^K$ [%]
(1)	(2)	(3)	(4)	(4)
<u><math>n = 1</math>: 1KE- (1KE-):</u>				
no significant detections (no significant detections)				
<u><math>n = 2</math>: 2KE- (2KE-):</u>				
HP 2	42 (45)	82 (94)	58 (75)	49 (80)
HP 4	43 (69)	97 (> 99.98)	31 (66)	39 (62)
HP 8	8 (70)	99.8 (99.8)	5 (32)	23 (41)
LB 32 8	28 (58)	88 (99.0)	29 (72)	27 (53)
LB 64 8	34 (64)	69 (96)	20 (60)	18 (34)
LB 64 16	18 (69)	98 (99.5)	10 (37)	28 (44)
<u>A2..3 (A2..5):</u>				
no significant detections (no significant detections)				
<u>M: <math>A_{1024} = 0.114</math> (<math>A_{1024} = 0.2</math>)</u>				
HP 2	39 (36)	94 (99.99)	42 (50)	32 (35)
HP 4	43 (47)	99.6 (> 99.99 $\star$ )	22 (25)	31 (32)
HP 8	11 (19)	99.96 (> 99.99 $\star$ )	7 (8)	18 (20)
LB 32 8	30 (35)	97 (> 99.99 $\star$ )	20 (22)	22 (23)
LB 64 8	34 (38)	91 (> 99.99 $\star$ )	15 (17)	14 (14)
LB 64 16	22 (30)	99.4 (> 99.99 $\star$ )	12 (13)	23 (25)
<u>&lt;M&gt;: <math>A_{1024} = 0.114</math> (<math>A_{40} = 0.114</math>)</u>				
HP 2	58 (59)	99 (56)	52 (44)	54 (44)
HP 4	77 (56)	99.87 (57)	54 (37)	50 (38)
HP 8	79 (62)	99.97 (55)	64 (29)	54 (52)
LB 32 8	78 (57)	99 (55)	54 (38)	51 (47)
LB 64 8	78 (58)	97 (55)	59 (38)	54 (43)
LB 64 16	76 (61)	99.7 (54)	64 (32)	55 (46)

We also process five additional modulated simulations, and apply the modulation only to the range of multipoles  $\ell \leq 40$ , leaving higher multipoles unmodulated, since the aforementioned work operated at much lower resolution.

The test is able to reject the modulation of the CMB of the amplitude  $A_{1024} = 0.114$  at a very high confidence level (99.9%) depending on the pixelization scheme. Note however, that this model modulates all scales equally.

Although in principle, the modulation will change the underlying power spectrum at scales where it was applied, we estimate (Appendix A 1 a) that any such effect for the modulation of  $A_{1024} = 0.114$  still remains in greatly consistent with the non-modulated simulations’ power spectrum, and hence the results given in Table II do not result from the underlying power spectrum discrepancies.

We are unable to reject the possibility of modulation with such amplitude applied only to the large scales ( $\ell \leq 40$ ). Such modulation is therefore consistent with the GRF field or unnoticed by the test (Table II). However, according to the best-fit  $\Lambda$ CDM model (assuming even a noiseless observation), the multipoles  $\ell \leq 40$  carry only about 24% of the map’s power. The possible modulation signals at these scales must also be

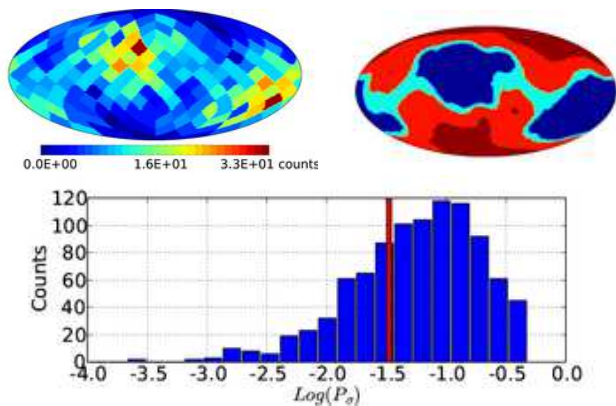


Fig 6: Histogram of the reconstructed modulation axis orientations as measured via the minimal joint probability  $P(\chi_q^2)$  (Eq. B7) in the set of 96 *LB 1 2 multi-masks* from 1000 modulated simulations (top-left) visualized using Healpix grid of resolution  $n_s = 4$ . The corresponding, reconstructed 50% (dark blue), 68% (light blue) and 95% (light red) confidence level contours obtained after smoothing the histogram with a Gaussian beam of FWHM =  $7^\circ$  (top-right). The reconstructed distribution is normalized on a hemisphere. In the bottom plot: the distribution of minimal log-probabilities ( $\log P(\chi_q^2)$ ) obtained from 1000 simulations modulated with amplitude  $A_{40} = 0.114$  along with the value obtained from the V map of the WMAP3 data.

more difficult to constrain as these are dominated by the cosmic variance uncertainty.

To investigate this further, we test simulations with only the large scales being modulated according to  $A_{40} = 0.114$  along direction  $(l, b) = (225^\circ, -27^\circ)$ . We filter out these scales up to  $\ell_{\max} = 40$  (using the Kp03 sky cut) in SH space and downgrade the map to  $n_s = 64$ , and process these using a new set of *multi-masks* of type: *LB 1 2* - i.e. having only two regions, each covering a hemisphere. We use 96 such *multi-masks* with orientations defined by the centres of pixels of the northern hemisphere in the ring ordering of the Healpix pixelization scheme of resolution  $n_s = 4$ . We prepare a set of 1 000 modulated simulations treated as data and use 1 000 independent GRF simulations to test the consistency with SI. We split the GRF simulations into two sets of 500 simulations each, to derive the covariance matrix, and probe the underlying  $\chi^2$  distribution.<sup>6</sup> We carry out the multi-region analysis using 96 *multi-masks LB 1 2*, and record the values of minimal probabilities (per modulated simulation) and the corresponding orientation of the *multi-mask*. The spatial distribution of these orientations defines the accuracy to reconstruct the correct intrinsic modulation field orientation at these scales, under cut sky and negligible amounts (at these scales) of noise.

The result is plotted in Fig. 6 (top-left). It is easily seen that while the direction is quite correctly found, the dispersion of the directions within even 50% CL contour (Fig. 6 top-right) is quite large which precludes a very precise determination of the modulation axis. We find, that statistically  $\sim 8\%$  (the probability corresponding to the peak value in the bottom plot in Fig. 6) of Gaussian simulations, to which we compare the modulated simulations treated as a data, exhibit a more unusual configurations of hemispherical variance distribution.

<sup>6</sup> Note that with the *LB 1 2 multi-masks* having only two regions it is not necessary to process a very large number of simulations to assess a good convergence.

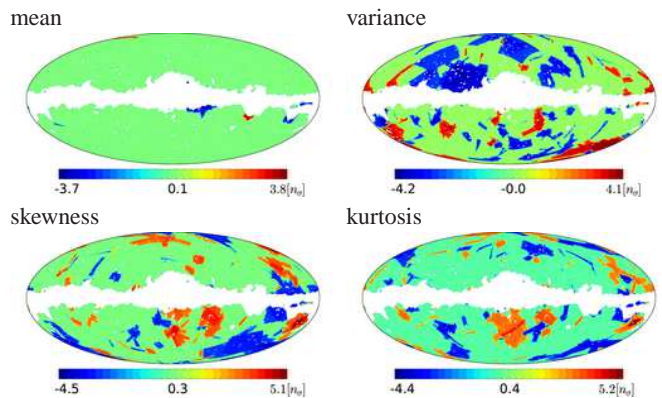


Fig 7: Results of the single-region analysis visualized in the composite  $n_\sigma$  maps of the INC data, for each of the MODs. The threshold of  $n_{\sigma,th} = 3$  (as defined in Sect. III D) is used. Mollweide projection and the galactic coordinates are used. The origin of the coordinate system  $(l, b) = (0, 0)$  is in center of the plots and the galactic longitude increases leftwards. Regions around the Galactic plane are partially removed by the Kp03 sky mask. The same convention is kept throughout the rest of this paper.

Consequently, we report this median rejection threshold of  $\sim 92\%$ , as the statistical sensitivity of the method for detecting the large scale modulation (i.e. in the filtered maps modulated with  $A_{40} = 0.114$ ). We consider this result - i.e. the low rejection confidence level - to be penalized mostly by the cosmic variance uncertainty and freedom of phases to assume an arbitrary orientations with respect to the (unsymmetrical) sky cut. Consequently, we note that due to these uncertainties, it may be difficult to increase this rejection level for scales of  $\ell_{\max} \sim 40$  and amplitude  $A = 0.114$ .

## V. APPLICATION TO WMAP THREE-YEAR DATA

We now present the results of the statistics described in Sect. III applied to the three-year and five-year WMAP data.

### A. Individual region statistics

The individual region statistics as described in Sect. III find numerous regions amongst our many pixelization schemes, which deviate by more than certain  $|n_{\sigma,th}|$  in all MODs. Table III gives an incomplete list of some of the strongest detections. In Fig. 7 we plot the detected regions at  $|n_{\sigma,th}| = 3$  in the individual region statistics of the INC data.

Note that with our approach the so-called “cold spot” is not detected at  $3\sigma$  level from being cold (i.e. via distribution of means) at all tested resolutions (Table III). It appears at about  $\sim 2.7\sigma$  around galactic coordinates  $(l, b) = (211^\circ, -57^\circ)$ . Excessively “cold” or “hot” deviations in all MODs are detected in general with large values of  $n_\sigma$ .

As expected the  $n_\sigma$  map of the means in Fig. 7 shows that the strongest deviating regions are directly close to the galactic plane cut off by the Kp03 mask, thus hinting at foreground residuals.

The variance  $n_\sigma$  map shows local strong anomalies with the extended variance suppression in the northern hemisphere towards  $(l, b) = (67^\circ, 19^\circ)$  and with an extended variance excess towards  $(l, b) = (199^\circ, -55^\circ)$ . We note that these local-



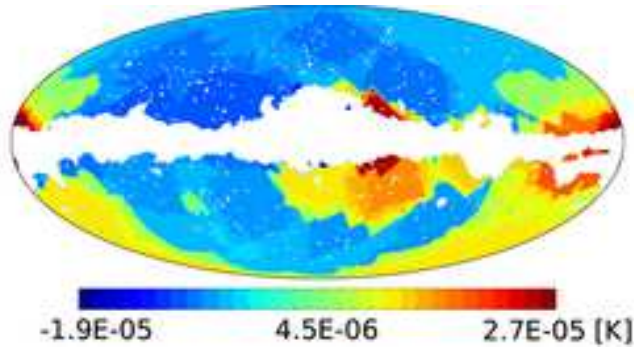


Fig 8: Results of the single region analysis. Residual difference ( $\Delta = \sqrt{\sigma^2} - \langle \sqrt{\sigma^2} \rangle$ ) scrambled map of the variance distribution in the INC map processed with 100 *multi-masks* of the *HP 2* pixelization scheme. The well known, large scale hemispherical power distribution asymmetry is clearly seen as is the distribution of foreground residuals along the galactic cut.

ized anomalies must, at least in a part, make up for the hemispherical power asymmetry.

Skewness and kurtosis maps consistently indicate strong local deviations from GRF simulations towards  $(l, b) = (193^\circ, -26^\circ)$  and  $(l, b) = (356^\circ, -36^\circ)$ . While some regions appear in all three maps, some appear only in one of the moments therefore the correlation between those results is not obvious.

In order to investigate the spatial distribution of this high  $n_\sigma$  regions, we plot in Fig. 8 the  $\Delta$  map, of differences between the variance distribution measured in each region of *multi-masks* of the *HP 2* pixelization scheme, and the simulations average,  $\Delta \equiv d_i = \sqrt{\sigma_i^2} - \langle \sqrt{\sigma_i^2} \rangle$ . The map is obtained by scrambling 100 difference maps from 100 different *multi-masks* (as described in Sect. III D). This map can be seen as a residual map for the local variance. This residual map exhibits a well known power asymmetry (Eriksen et al. 2007, 2004). The dipole ( $\ell = 1$ ) component of this residual masked map (ignoring the effect of the mask) is aligned along axis  $(l, b) = (237^\circ, -44^\circ)$  with power excess in the southern hemisphere. In order to probe this direction further, for each individual *multi-mask* we also produced an  $n_\sigma$  estimator maps and checked the orientation of the dipole axis. Fig. 9 shows the PDFs obtained for the orientation of the dipole asymmetry in galactic longitude and latitude. Interestingly, we notice that the orientation of the axis of the hemispherical power asymmetry has some scale dependence. When using smaller scales

Table III: An incomplete list of strongest deviation directions from maps in Fig 7 at  $|n_{\sigma,th}| = 3$  in the individual region analysis for means, variances, S and K, sorted in galactic longitude ascending order. Notice that with our simulations we directly probe the  $\pm 3.7\sigma$  PDF region without need for extrapolations.

mean		variance		skewness		kurtosis	
(l,b)	$n_\sigma$	(l,b)	$n_\sigma$	(l,b)	$n_\sigma$	(l,b)	$n_\sigma$
157, -29	-3.07	63, 28	-4.21	173, -73	-4.50	84, -31	-4.38
<b>211, -57</b>	<b>-2.78</b>	67, 19	-4.21	193, -26	5.06	195, -27	5.20
241, 42	-2.36	199, -55	4.13	209, 8	-3.50	<b>212, -55</b>	<b>-3.77</b>
265, -21	3.81	319, -27	3.40	217, 35	4.00	309, 59	-3.25
318, -9	-3.69			225, -20	-3.60	312, -21	3.65
167, 79	3.06			241, -52	-3.51	356, -36	4.25
				311, -20	3.86		
				357, -35	4.15		

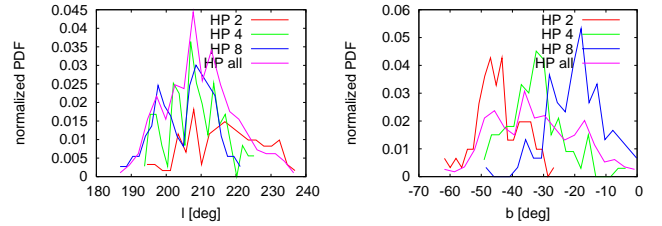


Fig 9: Orientation of the dipole component (galactic longitude - left panel and galactic latitude - right panel) of the  $n_\sigma$  maps for the INC map processed individually with all *HP* pixelization schemes. Each color corresponds to a different resolution of the pixelization scheme. While the longitudinal orientation of the dipole does not vary with resolution, the galactic latitude systematically shifts to lower galactic latitudes as resolution increases.

with finer pixelization schemes, the orientation of the power asymmetry dipole shifts from larger galactic latitudes (roughly from the position of the cold spot, with the mean PDF value  $(l, b) = (218^\circ, -43^\circ)$  – see also Table III) for the *HP 2* resolution to smaller latitudes  $(l, b) = (206^\circ, -18^\circ)$  for the *HP 8* pixelization scheme. The dependence of the power asymmetry orientation in function of the pre-filtered in SH space data have previously been tested by Hansen et al. (2004a). While we will return to the power asymmetry issue in the next subsections, we note that the medians of the dipole axis distributions of other MODs are not correlated with the dipole axis orientation of the variance map (Fig. 9) and generally point at some other locations.

In the next section we quantify the statistical significance of these deviations.

## B. Joint multi-region statistics

In Fig. 10 we plot a compilation of all joint “probabilities of exceeding”, calculated with all datasets considered (Q, V, W, and INC) in all 600 *multi-masks*. In order to visualize the smallest probabilities logarithmic scale is used. Note that we sort these probabilities in each MOD and dataset so as to ease visualization, so the points with same abscissa in different MOD and data sets do not necessarily correspond to the same *multi-mask*.

Most of the results concentrate along the zero point of the joint log-probabilities, which indicates a good consistency of the data with the simulations at relatively high CL. (The white region in the Fig. 10 encompasses CLs of up to  $3\sigma$ ;  $3\sigma$  and  $4\sigma$  regions are shaded in red and yellow respectively).

It is important to note that within one pixelization scheme the dispersion of probabilities in the Fig. 10 results only from the orientation of the *multi-mask*. As a result, the statistical method involving many pixelization schemes help us obtain the unbiased results that one could get relying only using a single pixelization scheme. We also recall that for each plotted point, the statistic was also calculated for  $N_{\text{simPDF}(\chi_q^2)} = 1000$  simulations in order to probe the underlying PDFs. For each point the corresponding full covariance matrix was obtained from  $N_{\text{sim}(C_q)} = 9000$  simulations (as described in Appendix B 2).

We now focus on three distinctive sets of results, based on the Fig. 10, and quantify the deviations in more detail. We detail on a tentative excess seen in kurtosis before focusing

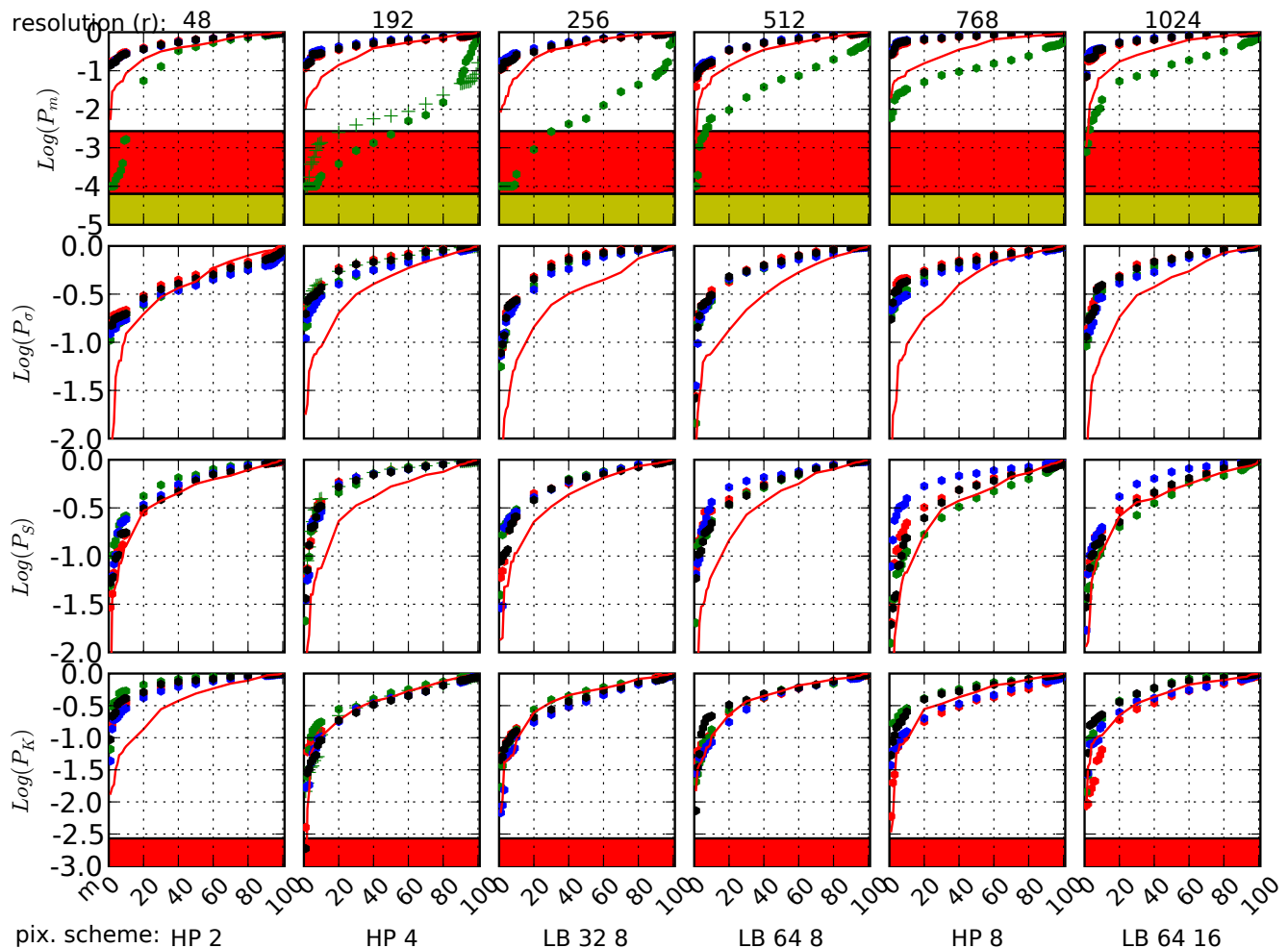


Fig 10: Results of the “multi-region” analysis. Dependence of joint probabilities of exceeding ( $P(\chi_q^2)$ , Eq. B7) as a function of *multi-mask* number for all pixelization schemes considered. The probabilities calculated with the spectral data maps from channels Q, V, W, INC are plotted in red, green, blue and black dots respectively. Each dot corresponds to the joint probability using one *multi-mask*. From the left to the right, the panels show results for increasing resolution of the pixelization scheme (see Table I) with 100 different *multi-masks* (along abscissa) in each. From top to bottom the four rows correspond to the four MODs - i.e. mean, variance, S and K respectively. Probabilities corresponding to the WMAP5 V5 data for pixelization scheme *HP 4* are plotted with green crosses (+).  $3\sigma$  and  $4\sigma$  confidence levels are shaded in red and yellow respectively. The joint probabilities were sorted in each dataset before plotting for better visualization; therefore the probabilities from different datasets generally do not correspond to the same *multi-mask* numbers and do not directly correspond to the unique reference numbers used in the analysis. Hence the most unlikely events are localized at the left side in each panel. Additionally we plot the thin red line, which indicates the distribution of probabilities obtained from 100 GRF simulations of the Q data, each of which was processed with one (different for each simulation) *multi-mask*. If the data follow the expectation of GRF then statistical departure of data from this line would manifest certain degree of correlation between probabilities obtained with different *multi-masks* for the same dataset (as discussed in Sect. VI). For better visualization in range  $m \in [10, 90]$  we plot only every 10<sup>th</sup> sorted probability value.

on the large scale power anomalies, and on unusually strong dipole contribution in the V channel of the WMAP. Then, we comment on the results from tests carried out with the difference map datasets.

### 1. Localized Kurtosis excess

In Fig. 10 there is one “ $3\sigma$ ” detection in kurtosis in *HP 4* pixelization scheme in the INC dataset (bottom second from the left panel in Fig. 10) – a result found using one in 100 of *multi-masks* probing these scales. Here we discuss this particular point as a tentative detection because although the *multi-mask* bins the data to create the most unlikely realization of the kurtosis, it lies in the low-end tail of the whole spectrum of equivalent measurements and hence its statistical impact can-

not be large.

Table IV: Three  $\sigma$  NG detections in K multi-region statistics of the INC data using *multi-mask* resulting in joint probability  $P(\chi_a^2) < 0.0027$  for the resolution  $n_s = 512$  and  $P(\chi_a^2) < 0.005$  for the resolution  $n_s = 64$ . The (l,b) field gives the galactic coordinates to the center of the region

region	resolution ( $n_s = 512$ )		resolution ( $n_s = 64$ )		(l,b)
	$N_{pix}$	$n_\sigma$	$N_{pix}$	$n_\sigma$	
160	2750	3.48	37	1.38	181, 2
185	12610	3.21	199	3.26	199, -23
104	16125	3.52	250	3.27	355, -44

In Fig. 11a we plot, thresholded at “ $3\sigma$ ”, the  $n_\sigma$  map using only this particular *multi-mask*. The details of the three most strongly deviating regions in this map are given in Table IV.

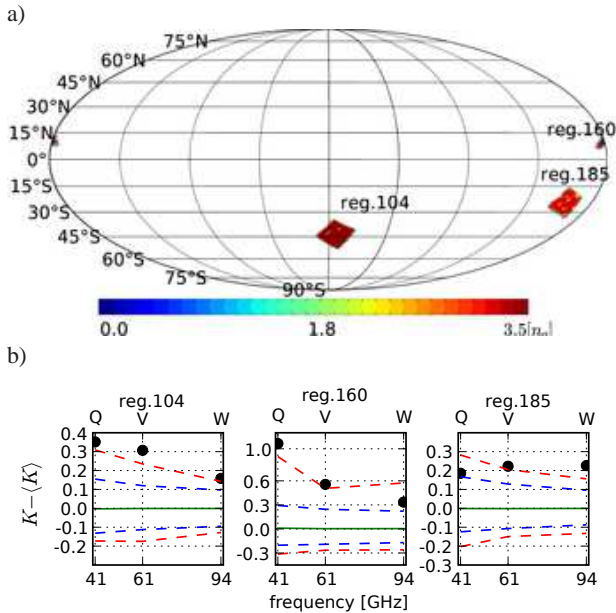


Fig 11: a) Kurtosis (thresholded at  $3\sigma$ )  $n_\sigma$  estimator map from the multi-region analysis of the INC data, inconsistent with GRF hypothesis at joint probability  $> 99.73\%$  CL. Only one *multi-mask no. 53* of the *HP 4* pixelization scheme) is used for this map, since only the one out of  $N_r N_m = 600$  yields  $|P(\chi_q^2)| < P_{th} = 1 - 0.9973$ . (See text and Table IV for more details). b) The spectral dependence of the kurtosis in the depicted regions in the three WMAP frequency bands along with the two and three sigma contours, from 1000 simulations, and the simulations mean are also plotted.

In case of two other *multi-masks*, using which the INC data yield a detection at confidence levels of 99% and 98% in K (*LB 64 8*) and S (*HP 8*) respectively, the “ $3\sigma$ ”-deviating regions turn out to be similarly located (like those in Fig. 11a). With these regions masked out from the analysis a good consistency with the GRF simulations is reached. Note that the region 160 is rather small – mostly removed by the galactic sky cut (see Fig. 11a and Table. IV for precise coordinates and size) however masking it has a comparable effect on the joint probability increase as masking out the two other and much larger regions. The consistency of the INC data with GRF simulations increases from 0.18% (without removal) to 1.1% and 0.9% with regions 160 and 104+185 removed respectively. Individual removal of regions 185 and 104 only increases the level of consistency by  $\lesssim 0.5\%$ . The simultaneous removal of all three regions increases the consistency up to 12%.

a. *Dependence as a function of multi-mask* To further test the robustness of this detection we have generated two other *HP 4* pixelization scheme sets of  $N_m = 100$  *multi-mask* each: one by simply choosing the three rotation angles with the prescriptions given earlier, and the other by focusing only on the region in the rotation angle parameter space within  $\pm 5^\circ$  around the original orientation of the *multi-mask* leading to the  $3\sigma$  detection.

With the first set we obtained results yielding a joint probability  $P(\chi_q^2) < 0.05$  with 3 *multi-masks*, while in the second we find that 25% of *multi-mask* yield  $P(\chi_q^2) < 0.05$ , and 4% yield  $P(\chi_q^2) < 0.01$ , with the strongest detection  $P(\chi_q^2) = 0.0035$ , of which the  $n_\sigma$  map points to the same three regions as depicted in Fig. 11a. We note that the reported regions (160 and 185) are located in directions towards

which the strongest deviations in the individual region statistics (Fig. 7) were found.

b. *Dependence as a function of frequency and resolution* In Fig. 11b we present the spectral dependence of kurtosis in the regions depicted in Fig. 11a. While there is a non-trivial spectral dependence in regions 160 and 185, with opposite tilt – red and blue respectively – there is almost no spectral dependence in region 104.

We also check the dependence on the S/N ratio in the selected regions. For this purpose we downgrade all datasets and simulations to resolution  $n_s = 64$ , which effectively increases the S/N ratio per pixel by a factor of 8. We redo the multi-region analysis lowering the minimal region pixel number threshold down to  $N_{pix} > 10$  and find that the minimal probability per *multi-mask* ( $P(\chi_q^2)$ ) corresponds to a rejection threshold of 99.5% CL (Table IV). As seen in Table IV the individual region response to the resolution change is strong only in case of region 160 while in the two other regions it is rather small. The result is robust under variations of region pixel number threshold and the number of simulations used to probe the underlying PDFs ( $N_{sim} \text{PDF}(\chi_q^2) \in \{1000, 5000\}$ ). Masking-out regions 104 and 185 reduces the anomaly to  $\sim 96\%$  CL and as expected in this case, removal of region 160 has basically no impact on this value.

c. *Summary* The non-trivial spectral dependence and close galactic-plane alignment in two of the three selected regions (160 and 185) suggests presence of some residual foreground anomalies. In case of the regions away from the galactic plane (104 and 185) since the local oddity is insensitive to the S/N ratio change it is also unlikely that an unknown instrumental noise fluke generates them. While we will return to the overall statistical significance of these findings in Sect. VC, we note that the positive KE seems to be inconsistent with the extended foregrounds interpretation of these detections, according to the results from Sect. IV. Also the  $3\sigma$  detection of the multi-region analysis appears only in the INC data, but is clearly weaker in other single band maps.

Given that this detection results from just one particular *multi-mask* and is selected from the lower-tail end of a whole distribution of equivalent measurements, it is inconclusive as regards indicating whether this detection is not just a fluke. Given that, we report in particular region 160, whose removal leads the overall significance to drop below  $3\sigma$  CL, as a tentative detection noting that more sophisticated local statistical analyses (see Sect. VI) could be invoked to back these results up or refute them.

## 2. Variance large scale distribution

In Sect. VA we analyzed the large scale power distribution as measured via *multi-masks* with regions of angular sizes ranging from  $6^\circ$  to  $30^\circ$  (Fig. 8 and Fig. 9).

In this section we focus on the joint multi-region analysis of the variance distribution. The corresponding results are illustrated in the second row of Fig. 10. The data remain in excellent consistency with the simulations.

In Sect. IVD we found that the modulation amplitude (defined by Eq. 3) of  $A_{\ell_{\max}=1024} = 0.114$  would be rejected at  $> 99.9\%$  CL, and we argued that the modulation parameter  $A_{\ell_{\max}=40} = 0.114$  would statistically be difficult to exclude at CL higher than 92%. Using our main set of the *multi-masks* (Table I) we fail to detect, in any of the data sets tested, any statistically significant anomaly, such as the claimed hemispher-

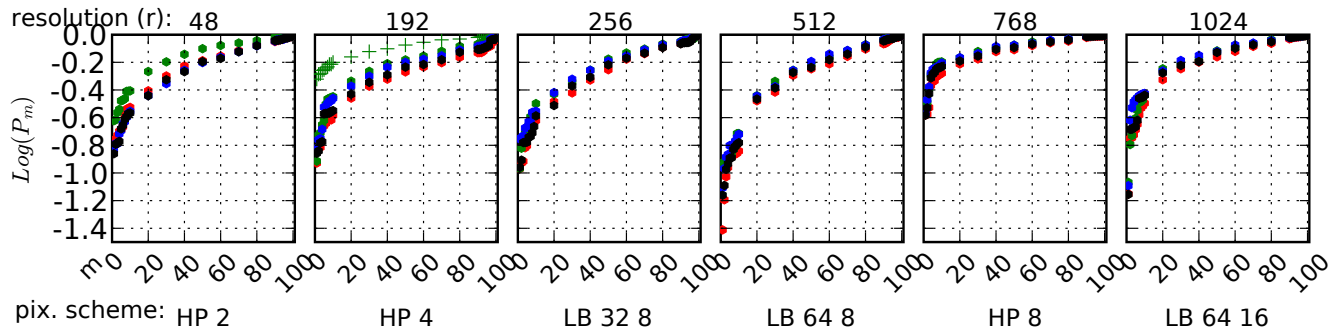


Fig 12: Results of the “multi-region” analysis with the dipole-corrected V (V5) data. Joint probabilities  $P(\chi_q^2)$  (Eq. B7) for 600 *multi-masks*. The probabilities calculated with the spectral data maps from channels Q, V, W, INC are plotted with red, green, blue and black dots respectively. WMAP5 V5 data are plotted with green crosses (+) in HP 4 only. The V dataset original dipole has been replaced by the simulated dipole and removed in case of V5 data. Each dot (cross) corresponds to the joint probability of one *multi-mask*. From left to the right, the panels show the results with increasing resolution of pixelization schemes (see Table I) with 100 different *multi-masks* in each panel. Only the “mean” data is shown since all other results remain almost unchanged. For better visualization in range  $m \in [10, 90]$  we plot only every 10<sup>th</sup> sorted probability value.

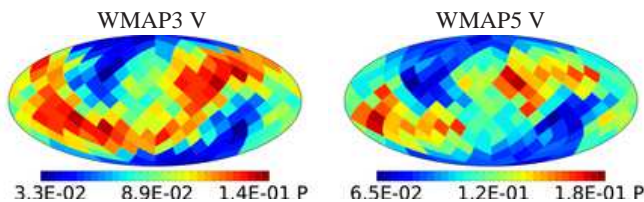


Fig 13: Results of the multi-region analysis, using the set of 96 *LB 1 2 multi-masks*, of the filtered in SH space up to  $\ell_{\max}=40$ , low-resolution V data (left), and V5 data (right). The color in each pixel encode the multi-region, joint “probability of exceeding” derived with the *LB 1 2 multi-mask* rotated to the direction of the center of that pixel. Note that half of pixels in each map is redundant.

ical power asymmetry (depicted in Fig. 8), as measured from the large scale variance distributions in the multi-region analysis.

As an extension to that, we repeat the analysis performed in Sect. IVD for the low resolution, filtered in SH space up to  $\ell_{\max}=40$ , WMAP data, using the same set of *LB 1 2 multi-masks*, to test the variance distributions in the corresponding set of 96 differently oriented hemisphere pairs. We thereby extend the test for the largest possible scales of  $180^\circ$ . We merge the Kp03 sky mask with the *LB multi-masks* for the analysis of the WMAP3 data, and KQ75 sky mask for analysis of the WMAP5 data. The result of the multi-region (here only two region) analysis is plotted in Fig. 13 for the V data (left) and V5 data (right). The minimal “probabilities of exceeding” found are:  $\min(P(\chi_q^2)) \approx 3.3\%$  (also marked in Fig. 6 bottom) towards  $(l, b) = (247.5^\circ, -30^\circ)$ <sup>7</sup> for the V data and  $\min(P(\chi_q^2)) \approx 6.5\%$  towards  $(l, b) = (281.5^\circ, -19^\circ)$  for the V5 data.

These two results agree well with the previously estimated (Eriksen et al. 2007) intrinsic modulation parameter value  $A = 0.114$  at scales  $\ell_{\max} \leq 40$ , as they lie well within “one-sigma” region of the distribution of log-likelihoods obtained from 1000 simulations modulated with the modulation

of  $A_{40} = 0.114$ . However we note that it will always be difficult to reject such modulation at high confidence level as it is also realized (to this or a greater extent) on average in  $\sim 8\%$  of GRF simulations (Sec. IVD).

Note that the distribution of the probabilities of the joint multi-region analysis (Fig. 13) has a very flat and extended maximum and, for example, the minimal joint-probability in the V data in the reported direction is only 0.2% smaller from the probability corresponding to the direction close to the galactic pole, which is roughly  $50^\circ$  away from the minimal probability direction.

Analogous analysis, involving the *LB 1 2 multi-masks*, but performed on the full resolution unfiltered WMAP V5 data, results in larger minimal-probabilities:  $\min(P(\chi_q^2)) \approx 9.6\%$  and the probability is minimized towards  $(l, b) = (225^\circ, -78^\circ)$ .

### 3. Residual dipole of the WMAP V channel.

In Fig. 10 we see a deviation in the distributions of the mean in the V dataset (green dots) and in V5 dataset (green crosses) for most of the *multi-masks*. The fact that it is visible in most *multi-masks* suggests that the anomaly is not particularly sensitive to the *multi-mask* orientation, and that it comes from large angular scales. Indeed, as measured by the  $n_\sigma$  values in individual regions of the *multi-mask* with the lowest joint probabilities, no region significantly deviates from simulations.

However, we find that the V data are fully consistent with the GRF simulations if we remove the dipole from the data, which is roughly  $\sim 2$  times larger than the one in our simulations<sup>8</sup>. Actually the dipole values in the datasets as measured by the multipoles  $l = 1$  on the Kp03 cut sky power spectrum are:  $47(\mu\text{K})^2$ ,  $54(\mu\text{K})^2$ ,  $45(\mu\text{K})^2$  in Q, V, W datasets respectively. The corresponding values in the WMAP5 data are:  $64(\mu\text{K})^2$ ,  $54(\mu\text{K})^2$  in V5 and W5 maps respectively. The measurements of dipoles on initially dipole-free maps, using a sky mask, introduce a bias

<sup>7</sup> This and the following result is accurate to within the tolerance of about  $\sim \pm 7^\circ$  resulting from the low-resolution search involving only 96 directions over a hemisphere in the HP 4 pixelization scheme.

<sup>8</sup> During the final stage of this work this sort of anomaly was independently reported in Eriksen et al. (2008)

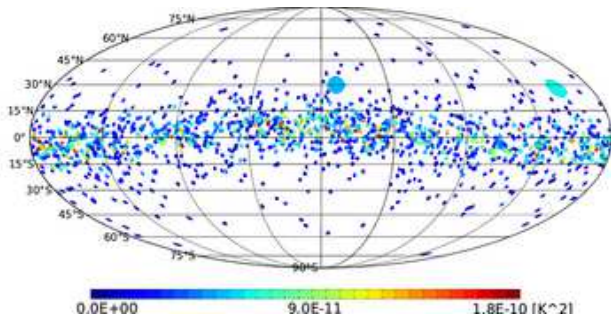


Fig 14: Distribution of dipole orientations generated due to Kp03 cut sky from 1467 full sky simulations with vanishing initial dipole. The large spot in the center (at the right-hand side) of the plot, indicates the orientation of the WMAP3 (WMAP5) V band dipole. The color scale reflects the amplitudes of the leakage generated dipoles.

due to power leakage from other coupled multipoles, leading to non-zero dipole amplitudes. When sky-cut-generated dipoles are statistically accounted for, the result would yield:  $20_{-26}^{+104}(\mu\text{K})^2$ ,  $27_{-26}^{+104}(38_{-26}^{+104})(\mu\text{K})^2$ ,  $18_{-26}^{+104}(27_{-26}^{+104})(\mu\text{K})^2$  in the WMAP3 (WMAP5) data at 95% CL, and hence is consistent with vanishing intrinsic dipole (except for the V band channel). We note that the noise component generates dipoles with amplitudes of order  $C_1 \sim 0.01(\mu\text{K})^2$  which is about three orders of magnitude less than the leakage effect. However the 95% CL effect is not sufficient to explain the strong anomalies detected in the regional tests.

The anomaly is more visible in the difference of dipole amplitudes between different channels. The difference of  $9 \pm 3(\mu\text{K})^2$  (at 95% CL) between channels V and W is excluded using simulations at  $> 99.9\%$  CL assuming that it is generated only by the power leakage from the cut sky. The difference in the WMAP V5 data is even larger:  $11 \pm 3(\mu\text{K})^2$ .

As for the amplitude of the V band dipole again, it becomes anomalous as one considers not only the magnitude, but also its orientation. The dipoles generated due to power leakage are strongly aligned within the galactic plane (Fig. 14) as a result of the shape of the Kp03 sky mask. While the Q and W dipoles measured on the cut sky are close from each other and close to the galactic plane pointing at  $(l, b) = (13^\circ, -8^\circ)$  and  $(l, b) = (7^\circ, 5^\circ)$  respectively, the dipole of the V band points at  $(l, b) = (350^\circ, 30^\circ)$  which is itself anomalous at  $> 97\%$  CL. WMAP5 data yield the dipole orientation  $(l, b) = (203^\circ, 28^\circ)$  (Fig. 14).

We note that all dipoles with  $b > 30^\circ$  have much smaller (roughly by an order of magnitude) amplitude than the one in the V band of the WMAP, which we believe is the reason for strong detections in the regional statistics carried out in the previous sections. When combining the alignment of the V band dipole with its magnitude, the hypothesis that it's generated only via the power leakage can be excluded at a very high CL since out of 1300 simulations, and within the subset of 37 that have generated dipole aligned at  $|b| > 30^\circ$  the maximal generated power is of only  $13(\mu\text{K})^2$  which makes even the CL estimation unfeasible, since this when compared to the  $54(\mu\text{K})^2$  of the V dataset ( $65(\mu\text{K})^2$  for V5), the simple  $\chi^2$  test implies a rejection basically without doubt to a very reasonable limits.

By reducing the dipole amplitude to the level consistent with simulations, or alternatively, by replacing it with our of our simulated dipoles, the data become consistent with our simulations at  $< 2\sigma$  CL in the joint multi-region analysis (see

Table V: Results of the all-*multi-masks* analysis for the signal dominated (co-added) and noise dominated (difference) maps. The columns content is as follows: (1) data set, (2) pixelization scheme, (3..5) “probability of rejecting” the consistency with GRF simulations (Sect. B 3) for each MOD. In case of V and V5 datasets, the probabilities for the data with corrected dipole component are given in brackets. We round to integer percentiles for probabilities  $< 99\%$ . The saturated values are marked with  $\star$ . We abbreviate the results consistent at given CL as: “no significant detections (CL)”.

d	Reg.sk.	$P_{rej}^m$ [%]	$P_{rej}^\sigma$ [%]	$P_{rej}^S$ [%]	$P_{rej}^K$ [%]
(1)	(2)	(3)	(4)	(4)	(5)
INC	ALL		no significant detections (68%)		
Q	ALL		no significant detections (68%)		
V	HP 2	59 (20)			
	HP 4	99.8 (35)			
	HP 8	88 (16)	no significant detections (68%)		
	LB 32 8	99.5 (30)			
	LB 64 8	94 (37)			
	LB 64 16	86 (24)			
V5	HP 4	99.3 (15)	no significant detections (68%)		
W	ALL		no significant detections (68%)		
QV	ALL	$> 99.9^\star$			
VW	ALL	$> 99.9^\star$	no significant detections (95%)		
QW	ALL	$> 99.9^\star$			

Fig. 12) and at  $< 1\sigma$  CL in all-*multi-masks* analysis at all resolutions (see Table V in the next section). Note that the presence of this dipole in the V band is of no cosmological consequences since the dipole is marginalized over for any cosmological analysis, but may be important for other low- $\ell$  analyses.

### C. All-*multi-masks* analysis

We now discuss the result of the all-*multi-masks* analysis described in Sect. B 3. The corresponding results are presented in Table V. We see that the data are consistent with the simulations at  $\sim 68\%$  CL. The previously mentioned (in Sect. V B 1) tentative NG detection in the INC data in kurtosis has indeed the largest probability of rejecting across the scales (61%) but it turns out to be statistically completely insignificant.

The large scale variance distribution is found to be perfectly consistent with the GRF simulations.

We find a significant anomaly in the dipole component of the V band channel (see also Sec. V B 3) detected via distribution of means in both WMAP3 (99.8% CL) and WMAP5 (99.3% CL) data.

All of the difference maps (see Sect. V E) show a very strong departures from foregrounds free, simulated, difference maps, most prominently detected in means distributions.

### D. The “cold spot” context

A NG anomalous kurtosis excess of a wavelet convolution coefficients has been reported (e.g. Cruz et al. (2007)) in the southern hemisphere, and was found to be associated with the locally cold spot (CS) in the CMB fluctuations around galactic coordinates  $(l, b) = (209^\circ, -57^\circ)$ . In that work the wavelet convolution scales ranging from  $\sim 6.6^\circ$  to  $\sim 13.2^\circ$  in diameter were used, with anomaly being maximized at scales of  $\sim 10^\circ$  with a rejection on grounds of Gaussianity assumption

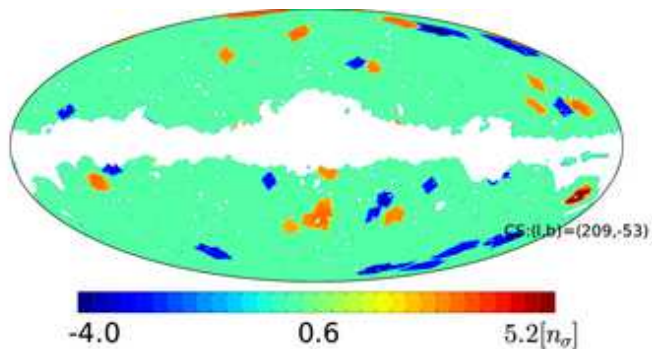


Fig 15: Kurtosis  $n$ -sigma map, thresholded at  $n_{\sigma,th} = 3$ , combined from 100 *multi-mask* of the *HP 8* pixelization scheme. The “cold spot” is marked with “CS”.

exceeding 99% CL. At the same time the authors note that the CS was not detected in the real space analyses.

The range of scales mentioned correspond roughly to the scales tested by the *HP 4* ( $\sim 14.6^\circ$ ) and *HP 8* ( $\sim 7.3^\circ$ ) pixelization schemes (see. Table I).

In Fig. 15 we plot the scrambled  $n$ -sigma map of kurtosis from the single-region analysis, obtained from 100 *multi-masks* of the *HP 8* pixelization scheme, which most closely corresponds to the scales, at which the CS was detected. The deviation of  $-3.6\sigma$  in the “the cold spot” direction, centered at  $(l, b) = (209^\circ, -53^\circ)$  in Fig. 15 is clearly found with many other, locally significant, deviations. This particular CS however is not found at the same location in e.g. *HP 4* pixelization schemes or in skewness  $n$ -sigma maps, but rather it is shifted towards smaller galactic longitudes.

As an extension to the tested scales, in this section we run a high resolution test using pixelization scheme *HP 16* corresponding roughly to scales of  $\sim 3.7^\circ$  and the INC data. We use 10 additionally generated *multi-masks* in this resolution, and we perform the single region, joint multi-region, and all-*multi-masks* statistics. We also performed the same analysis using the filtered up to  $\ell_{max} = 40$  is SH space, low resolution ( $n_s = 64$ ) maps in which the spot is clearly visible.

Although we find a locally negative KE and positive excursions from expected distributions by  $\gtrsim 3\sigma$  around the CS direction in variance, we also find similar excursions at several other directions. The CS itself is well localized in the scrambled  $n$ -sigma maps of means with minimal value  $-2.9$ .

However, none of these detections (see also Fig. 7) hold under the scrutiny of the multi-region and all *multi-masks* analyses (Table V), that find these local anomalies to be statistically insignificant.

### E. Differential maps tests

We discuss results of the QV, VW and QW difference maps tests as a simple cross-check with the CMB signal dominated maps tests, and a rough estimation of the residual foregrounds amplitude. We limit the number of *multi-masks* to 10 and use  $N_{sim} = 10^4$  simulations in single region analysis and  $N_{simPDF}(\chi^2_p) = 10^3$  ( $N_{sim(C_p)} = 9 \cdot 10^3$ ) simulations in joint multi-region analysis as before.

As shown in Table V the residual foregrounds are very strongly ( $> 99.9\%$  CL) detected in all difference maps, due to anomalies in means distributions. In particular the  $n$ -sigma and difference ( $\Delta = m - \langle m \rangle$ ) maps of means distributions

Table VI: Residual foregrounds amplitudes in the cross-band difference maps. The columns contain: (1) pixelization scheme, (2) approximate angular size of the region as inferred from number of regions, (3) approximate corresponding multipole number  $\ell = 180/\Omega_{reg}$ , (4..6) - standard deviation of the difference maps outside Kp03 sky mask.

Reg.sk.	$\Omega_{reg}$ [deg]	$\ell$	$\sigma(QV)$ [ $\mu K$ ]	$\sigma(VW)$ [ $\mu K$ ]	$\sigma(QW)$ [ $\mu K$ ]
(1)	(2)	(3)	(4)	(5)	(6)
<i>HP 2</i>	29.3	6	2.7	1.9	3.8
<i>HP 4</i>	14.6	12	3.0	3.0	4.7
<i>LB 32 8</i>	12.7	14	3.9	3.5	5.1
<i>LB 64 8</i>	9.0	20	4.7	4.6	6.0
<i>HP 8</i>	7.3	25	4.9	4.9	6.2
<i>LB 64 16</i>	6.3	29	5.8	6.0	7.2

in QV, most prominently exhibit a dipole like structure oriented roughly at  $(l, b) = (260^\circ, 60^\circ)$  which is close to the kinetic dipole direction (Fig. 16a). The VW  $n_\sigma$  map has a similar dipole structure, but with opposite orientation, which however is absent in the QW  $n_\sigma$  map. We find this to be a consequence of the previously detected (Sect. VB 3) anomalous dipole component of the V band channel. Removing the dipole components from the difference maps, we have redone the three stages of the analysis, and although the dipole structure ceased to dominate, we still find a very high ( $> 99.9\%$  CL) rejection probabilities for in means as quoted in Table V.

In Table VI we present the amplitudes of the residual foregrounds as measured by the variance of the  $\Delta$  difference maps of means distribution for different scales as probed by our pixelization schemes. These remain in a good consistency with the limits given in Bennett et al. (2003) for residual foregrounds contamination.

In Fig. 16(c-h) we show the  $n_\sigma$  maps with distribution of the regions in the difference maps outstanding from simulations at significance larger than  $3\sigma$  (i.e. we use  $n_{\sigma,th} = 3$ ). Clearly, the close galactic plane regions are strongly detected. We note that the the KQ75 sky mask partially removes the most affected regions around  $(l, b) = (233^\circ, -10^\circ)$ ,  $(l, b) = (259^\circ, 18^\circ)$  and the previously-mentioned  $(l, b) = (199^\circ, -23^\circ)$ .

It is interesting to note that the largest scale negative ( $n_\sigma < 0$ ) anomalies seen in *HP 2* (Fig. 16c-d) away from the galactic plane, can also be induced by the foregrounds dominating along the galactic plane (with  $n_\sigma > 0$ ) due to a very strong linearity of foregrounds induced quadrupoles with strong maximums aligned along the galactic plane and consequently strong minimums allocated close to the poles (Fig. 16b). Such mechanism of foregrounds-generated linearity of the quadrupoles of the difference maps will not work in the foregrounds-free simulations, adding thereby to the observed large scale anomalies as probed via the largest regions. This effect is considerably smaller in the higher resolution pixelization schemes.

In order to test the consistency of our noise simulations with the noise of the WMAP data, and the approximation the uncorrelated, white noise and to constrain limits of the systematical uncertainties, we also performed analysis using Q12 and V12 difference maps in *HP 2* pixelization scheme. The details of this analysis is given in Appendix C. Here, we briefly report the result that the systematical effects measured, as before, by the standard deviation of the difference  $\Delta$  maps remains at level  $< 1.7\mu K$  at the scales corresponding the *HP 2* pixelization scheme i.e.  $\gtrsim 30^\circ$ .

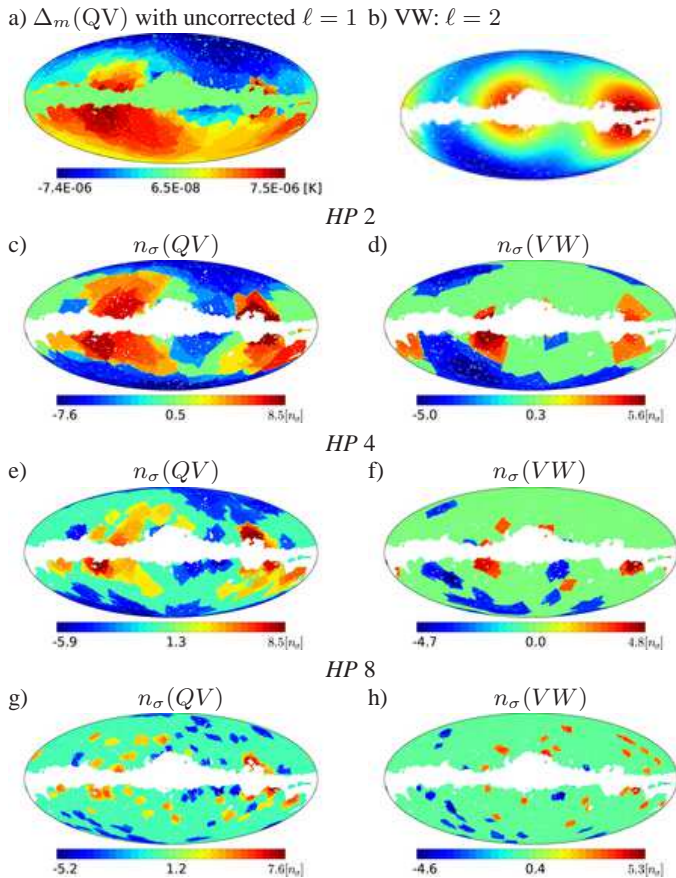


Fig 16: Results of the single-region difference maps analysis. In panel a) the residuals ( $\Delta_m(QV) = m - \langle m \rangle$ ) for the difference QV data, uncorrected for the anomalous V band dipole is plotted. In panel b) the quadrupole of the VW difference map and in panels c) through h) for the three *HP* pixelization schemes, we plot the thresholded at  $3\sigma$ ,  $n_\sigma$  maps of means distributions of the differential datasets QV (left) and VW (right) with the anomalous dipole component removed from the data. We make these maps (and maps of higher MODs) publicly available at <http://cosmo.torun.pl/~blew/SKregstat/>

## VI. DISCUSSION

### A. Sensitivity, correlations and extensions

Although we have shown that the statistics is rather helpless to robustly detect the NG signals considered (defined in Sec. IV B) via MODs higher than the variance, the statistics also proved to be a sensitive and precise tool for statistical isotropy measurements via variance and means. While we fail to detect the NG templates (inducing signals of rms  $\sim 100\mu\text{K}$  within spots of  $\sim 10^\circ$  via skewness and kurtosis) in the multi-region NG analysis, the single region analysis detects these as locally significant ( $n_\sigma \gtrsim 3$ ). Instead such template can be detected in the all-*multi-masks* analysis at  $> 99.8\%$  CL via variance.

In Eriksen et al. (2004) a regional statistical analysis was performed using a set of circular regions uniformly distributed across the sky. Our analysis is similar in spirit but uses different statistics and a richer sets of regions, varying both in size and shape. This approach has been validated by the fact that we have shown that the resulting statistical signal can be a sensitive function of the particular choice of regions. This is most

prominently seen in case of the reported dipole anomaly in the V band of the WMAP data (Fig. 10), where it is easily seen that depending on the choice of the pixelization scheme (e.g. such as those associated with the results at the right-hand side of the top plots in Fig. 10) the obviously strong anomaly can be overlooked.

It is important to mention the correlations between various *multi-masks*. This correlation occurs since, although the *multi-masks* sample the data differently, in the end, the same data are being sampled. The degree of redundancy is directly connected to the number of *multi-masks* used in the analysis and the magnitude of the correlation is related to the size of the regions used in a pixelization scheme. To quantify this we carried out a simple statistical test only whose goal was to establish whether our test is statistically more sensitive to the change of the tested data itself or to the change of the *multi-masks* for various resolutions parameter  $r$  and MOD.

If the results from different *multi-masks* were strongly correlated, then for a constant number of DOF one would expect the variance of the results measured over these *multi-masks* (e.g.  $\chi^2$  values) to be much smaller than the variance computed while fixing a *multi-mask* but varying dataset. On the other hand, if the variance of the results when changing dataset was much smaller than the variance when changing *multi-mask*, then the test would not be very sensitive to particular features in the data, or even unstable. To test this we calculated the  $R$  statistic defined as follows:

$$R(r, \text{MOD}) = \frac{\langle \sigma_{\text{sim}}(\chi^2(r, \text{MOD})/\text{DOF}_{\text{eff}}) \rangle_m}{\langle \sigma_m(\chi^2(r, \text{MOD})/\text{DOF}_{\text{eff}}) \rangle_{\text{sim}}} \quad (4)$$

where  $\langle \rangle_{\text{sim}}$  denotes an average over simulations and  $\langle \rangle_m$  denotes an average over *multi-mask* for a given simulation, and where  $\text{DOF}_{\text{eff}} = \text{DOF}(r, m)$  is the effective number of degrees of freedom. Measuring this  $R$  statistic using our simulations, we find that the test is approximately equally sensitive at all resolutions and for all MODs, and that eventually it is little more sensitive to the change of the data under test than to the change of the *multi-mask* giving  $R$  values around 1.2.

The approach with arbitrary shape of the regions (*multi-mask*) and their orientation is quite flexible, and different shapes can possibly be used for different applications independently of the enforced sky cuts. This allows for a thorough test of the multivariate nature of this Gaussian field. One could also consider other statistics than the first MODs, as e.g. regional Minkowski functionals. Another possible extension is to apply a specific pre-filtering of the data in the SH space in order to expose for the test features dominating at particular scale. Such slicing of the data into subsets of maps according to some chosen ranges of multipoles could in principle significantly improve the sensitivity. The multi-region full-sky analysis though is restricted generally to the resolutions up to which the full covariance matrix analysis is feasible.

## VII. CONCLUSIONS

We introduce and perform a regional, real space test of statistical isotropy and Gaussianity of the WMAP CMB data, using a one-point statistics. We use a set of regions of varying size and shape (which we call *multi-mask*) allowing for an original sampling of the data. For each of the regions we

analyze independently or simultaneously, the first four moments of distribution of pixel temperatures (i.e. mean, variance, skewness and kurtosis).

We assess the significance of our measurements in three different steps. First we look at each region independently. Then we consider a joint multi-region analysis to take into account the spatial correlations between different regions. Finally we consider an “all-*multi-masks*” analysis to assess the overall significance of the results obtained from different sky pixelizations.

We show that the results of such multi-region analyses strongly depend on the way in which the sky is partitioned into regions for the subsequent statistics and that our approach offers a richer sampling of the underlying data content. Consequently the all-*multi-masks* analysis provides a more robust results, avoiding possible biases resulting from an analysis constrained only to a single choice of pixelization scheme.

We find the three-year WMAP maps well consistent with the realistic, isotropic, Gaussian Monte-Carlo simulations as probed by regions of angular sizes ranging from  $6^\circ$  to  $30^\circ$  at 68% confidence level.

We report a strong, anomalous (99.8% CL) dipole “excess” in the V band of the three-year WMAP data and also in the V band of the WMAP five-year data (99.3% CL) (Sect. VB 3).

We test the sensitivity of the method to detect particular CMB modulation signals defined via the scale dependent modulation amplitude parameter ( $A_{\ell_{\max}}$ ) for the case of modulation extending up to maximal multipole number of  $\ell_{\max} = 40$  and  $\ell_{\max} = 1024$ . We are able to reject the modulation of amplitude of  $A_{1024} = 0.114$  at  $> 99.9\%$  CL and find that  $A_{40} = 0.114$  can be statistically excluded only at  $\sim 92\%$  CL (Sect. IVD, VB 2). Given the WMAP V band data, we find that the large-scale hemispherical asymmetry is not highly statistically significant in the three-year data ( $\sim 97\%$ ) nor in the five-year data ( $\sim 93.5\%$ ) at scales  $\ell \leq 40$ . Including a higher- $\ell$  multipoles only decreases the significance of hemispherical variance distribution asymmetry.

We also test the sensitivity to detect a broad range of small ( $10^\circ$  in radius) locally introduced NG signals, inducing non-vanishing kurtosis (and in general skewness) of rms amplitude  $\sim 100\mu\text{K}$  and find that the method is able to detect these as locally significant, but the overall impact in the joint multi-region analysis is unnoticed by mean, skewness and kurtosis, but is strongly detected ( $\sim 99.8\%$  CL) by variance distributions. We conclude that the NG foreground-like signals will be easier to detect using local variance measurements rather than higher moments-of-distribution.

We also analyze our results in context of the significance of the “cold spot” (CS), reported as highly anomalous at scales corresponding to  $\sim 10^\circ$  in diameter. While we notice the cold spot region as having locally anomalous, negative kurtosis-excess and locally increased variance (eg. Figs. 7, 15), we do not find these deviations to be globally statistically significant.

We easily detect the residual foregrounds in cross-band difference maps at average rms level  $\lesssim 7\mu\text{K}$  (at scales  $\gtrsim 6^\circ$ ) and limit the systematical uncertainties to  $\lesssim 1.7\mu\text{K}$  (at scales  $\gtrsim 30^\circ$ ) as a result of the analysis of same-frequency difference maps. These levels are consistent with the previously estimated limits.

#### Acknowledgements

BL is grateful to Olivier Doré for useful comments, discussions, and encouragement. BL would like to thank Naoshi Sugiyama for his support and Boudewijn Roukema for careful reading of the manuscript. BL would also like to thank the anonymous referee for useful comments and suggestions. BL acknowledges the use of the Luna cluster of the National Astronomical Observatory (Japan), computing facilities of the Nagoya University and support from the Monbukagakusho scholarship.

We acknowledge the use of the Legacy Archive for Microwave Background Data Analysis (LAMBDA). Support for LAMBDA is provided by the NASA Office of Space Science.

- 
- Astier, P. et al. 2006, *Astron. Astrophys.*, 447, 31, [astro-ph/0510447]  
 Bartolo, N., Komatsu, E., Matarrese, S., & Riotto, A. 2004, *Phys. Rep.*, 402, 103, [astro-ph/0406398]  
 Bennett, C. L., Halpern, M., Hinshaw, G., et al. 2003, *ApJS*, 148, 1, [astro-ph/0302207]  
 Bernui, A., Mota, B., Rebouças, M. J., & Tavakol, R. 2007, *A&A*, 464, 479, [astro-ph/0511666]  
 Cabella, P., Hansen, F. K., Liguori, M., et al. 2006, *MNRAS*, 497  
 Cabella, P., Liguori, M., Hansen, F. K., et al. 2005, *MNRAS*, 358, 684  
 Cayón, L., Jin, J., & Treaster, A. 2005, *MNRAS*, 362, 826  
 Chiang, L.-Y., Naselsky, P. D., Verkhodanov, O. V., & Way, M. J. 2003, *ApJ*, 590, L65  
 Cole, S. et al. 2005, *Mon. Not. Roy. Astron. Soc.*, 362, 505, [astro-ph/0501174]  
 Copi, C. J., Huterer, D., Schwarz, D. J., & Starkman, G. D. 2006, *MNRAS*, 367, 79  
 Copi, C. J., Huterer, D., & Starkman, G. D. 2004, *Phys. Rev. D*, 70, 043515 (arXiv:astro-ph/0310511)  
 Cruz, M., Cayón, L., Martínez-González, E., Vielva, P., & Jin, J. 2007, *ApJ*, 655, 11, [astro-ph/0603859]  
 de Oliveira-Costa, A., Smoot, G. F., & Starobinsky, A. A. 1996, *ApJ*, 468, 457  
 de Oliveira-Costa, A., Tegmark, M., Zaldarriaga, M., & Hamilton, A. 2004, *Phys. Rev. D*, 69, 063516, [astro-ph/0307282]  
 Durrer, R., Juskiewicz, R., Kunz, M., & Uzan, J.-P. 2000, *Physical Review D*, 62, 021301  
 Eisenstein, D. J. et al. 2005, *Astrophys. J.*, 633, 560, [astro-ph/0501171]  
 Eriksen, H. K., Banday, A. J., Górski, K. M., Hansen, F. K., & Lilje, P. B. 2007, *ApJ*, 660, L81, [astro-ph/0701089]  
 Eriksen, H. K., Dickinson, C., Jewell, J. B., et al. 2008, *ApJ*, 672, L87, [arXiv:0709.1037]  
 Eriksen, H. K., Hansen, F. K., Banday, A. J., Górski, K. M., & Lilje, P. B. 2004, *ApJ*, 605, 14  
 Ferreira, P. G., Magueijo, J., & Gorski, K. M. 1998, *ApJ*, 503, L1+  
 Gaztañaga, E. & Wagg, J. 2003, *Phys. Rev. D*, 68, 021302  
 Gaztañaga, E., Wagg, J., Multamäki, T., Montaña, A., & Hughes, D. H. 2003, *MNRAS*, 346, 47  
 Górski, K. M., Hivon, E., Banday, A. J., et al. 2005, *ApJ*, 622, 759, [astro-ph/0409513]  
 Hajian, A. & Souradeep, T. 2006, *Phys. Rev. D*, 74, 123521, [arXiv:astro-ph/0607153]  
 Hansen, F. K., Banday, A. J., & Górski, K. M. 2004a, *MNRAS*, 354, 641, [arXiv:astro-ph/0404206]  
 Hansen, F. K., Cabella, P., Marinucci, D., & Vittorio, N. 2004b, *ApJ*, 607, L67, [arXiv:astro-ph/0402396]  
 Hartlap, J., Simon, P., & Schneider, P. 2007, *A&A*, 464, 399, [astro-ph/0608064]



Hinshaw, G., Barnes, C., Bennett, C. L., et al. 2003, *ApJS*, 148, 63, [astro-ph/0302222]  
 Hinshaw, G., Nolta, M. R., Bennett, C. L., et al. 2007, *ApJS*, 170, 288, [astro-ph/0603451]  
 Hinshaw, G. et al. 2007, *Astrophys. J. Suppl.*, 170, 288, [astro-ph/0603451]  
 Land, K. & Magueijo, J. 2005a, *Phys. Rev. D*, 72, 101302, [astro-ph/0507289]  
 Land, K. & Magueijo, J. 2005b, *MNRAS*, 362, 838  
 Magueijo, J. & Medeiros, J. 2004, *MNRAS*, 351, L1  
 McEwen, J. D., Hobson, M. P., Lasenby, A. N., & Mortlock, D. J. 2006a, *MNRAS*, 371, L50, [astro-ph/0604305]  
 McEwen, J. D., Hobson, M. P., Lasenby, A. N., & Mortlock, D. J. 2006b, *MNRAS*, 369, 1858, [astro-ph/0510349]  
 Naselsky, P., Chiang, L.-Y., Olesen, P., & Novikov, I. 2005, *Phys. Rev. D*, 72, 063512  
 Page, L. et al. 2007, *Astrophys. J. Suppl.*, 170, 335, [astro-ph/0603450]  
 Park, C.-G. 2004, *MNRAS*, 349, 313, [arXiv:astro-ph/0307469]  
 Riess, A. G. et al. 2004, *Astrophys. J.*, 607, 665, [astro-ph/0402512]  
 Schwarz, D. J., Starkman, G. D., Huterer, D., & Copi, C. J. 2004, *Physical Review Letters*, 93, 221301  
 Shandarin, S. F. 2002, *MNRAS*, 331, 865  
 Spergel, D. N. et al. 2007, *Astrophys. J. Suppl.*, 170, 377, [astro-ph/0603449]  
 Tegmark, M. et al. 2006, *Phys. Rev.*, D74, 123507, [astro-ph/0608632]  
 Vielva, P., Martínez-González, E., Barreiro, R. B., Sanz, J. L., & Cayón, L. 2004, *ApJ*, 609, 22  
 Wu, J. H. P., Balbi, A., Borrill, J., et al. 2001, *Physical Review Letters*, 87, 251303

## Appendix A: WMAP SIMULATIONS

### 1. Signal and noise pseudo $C_\ell$ tests.

In order to assess the confidence levels we have performed Monte-Carlo simulations of the signal ( $\ell_{max} \leq 1024$  and  $C_{0,1} = 0$ ) and inhomogeneous but uncorrelated Gaussian noise maps for all DAs, according to the best fit to the  $\Lambda$ CDM model power spectrum, extracted from observations (Hinshaw et al. 2007). The simulations include the WMAP window functions for each DA. The  $N_{sim} (= 10^4)$  full sky simulations were generated at the *HEALPIX* resolution  $n_s = 512$ , for each DA and preprocessed in the same way as the data.

In Fig. 17 an example of simulated, and recovered pseudo- $C_\ell$  is compared with the pseudo- $C_\ell$  of the WMAP data from channel Q1 as a simple consistency check. Similar simulations were performed for the remaining DAs.

As a simple consistency test, we present in Fig. 18 statistics of the full sky WMAP third year data as compared with the simulations. The data are well consistent with the simulations.

#### a. Tests of modulated-simulations' power spectrum

As mentioned in Section IV D the modulation (Eq. 3) alters the underlying power spectrum of the modulated simulations and could possibly mislead us in the interpretation of the high rejection confidence level thresholds, reported in Table II for the modulated simulations, since the additional power could be merely a result of the inconsistency on grounds of the

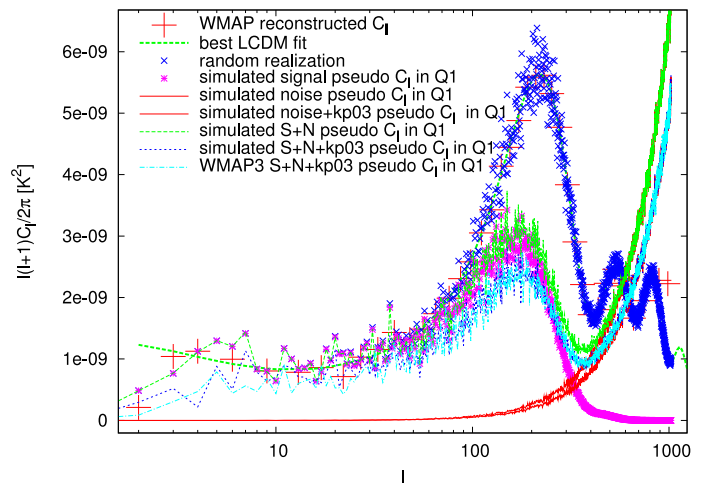


Fig 17: Consistency check between the simulations and WMAP three-year observations. The pseudo- $C_\ell$  power spectra of the WMAP (light blue/dot-dashed curve) and its simulation (the underlying blue/dashed line) in channel Q1 are well consistent both in Kp03 sky cut regime and in the noise dominated regime. Reconstructed power spectrum of the Hinshaw et al. (2007) is plotted as big red crosses.

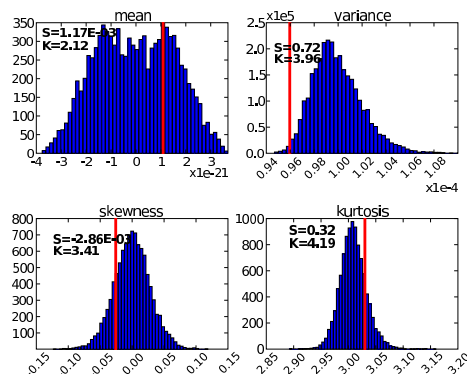


Fig 18: The distributions of means, variances, skewness and kurtosis of  $N_{sim} = 10^4$ , full sky, INC simulated data realizations, calculated outside the Kp03 sky mask. Skewness and kurtosis values of the distributions are also given. Vertical bars indicate the values derived from the WMAP three-year data. The quantile probabilities of the mean, variance, S, and K values of the WMAP data are  $\{0.57, 0.015, 0.34, 0.35\}$  respectively – well consistent with Gaussian, random simulations. Low probability of the total variance results primarily from the low quadrupole (octupole) of the WMAP data as compared with the best fit  $\Lambda$ CDM model. Note that the distribution of the means of the simulations represents only a numerical noise since during preprocessing all maps were shifted to zero the mean outside the Kp03 sky mask ( $\langle T \rangle \rightarrow 0$ ) and therefore it does not carry any important cosmological information. The spectral analysis yields a similar results.

intrinsic power spectrum mismatch, rather than the regional variance distribution analysis, and violation of the statistical isotropy.

In this section we quantify this effect. We generate a set of 10 WMAP V3 simulations and modulate their CMB component using modulations  $A_{1024}(\hat{n} = (225^\circ, -27^\circ)) = \{0.114, 0.2\}$ . We next extract their Kp03 cut sky pseudo-power spectra up to  $\ell_{max} = 700$  i.e. up to the scales where the noise component already strongly dominates over any possible CMB modulation signals. We derive the contribution to the total

variance of the map per multipole according to:  $\sigma_\ell = \frac{2\ell+1}{4\pi} C_\ell$  ( $\ell \in \{2, \dots, 700\}$ ). We measure the degree of the consistency of the modulated simulations' power spectra with the non-modulated simulations' power spectra, using the unbiased estimator of the full covariance matrix  $\Sigma_{ll'} = \text{Cov}(\sigma_\ell, \sigma_{\ell'})$  derived from 3000, analogously prepared  $\sigma_\ell$  vectors extracted from the GRF WMAP V3 simulations, and using the corresponding Monte-Carlo probed  $\chi^2$  values distribution from 223 additional simulations.

We find that the average rejection thresholds for the modulations  $A_{1024} = 0.114$  and  $A_{1024} = 0.2$  are 54% and 59% respectively with the standard deviation  $\sim 30\%$  in both cases. We therefore conclude that our results given in Table II cannot result from simply alteration of the power spectra after the modulation field has been introduced. Similar results are obtained if the off-diagonal terms of the covariance matrix are neglected, which indicates that the low detection threshold does not result from the limited number of simulations and a possible non-convergence of the covariance matrix.

## Appendix B: ASSESSING STATISTICAL SIGNIFICANCE

In this appendix we give details on our statistical approaches. For fast reference, we summarize the principal symbols used in Table: VII.

### 1. Individual region analysis

In the case of individual regions statistics for every  $i$ th region ( $i \in \{1, \dots, N_{reg}(r, m)\}$ ) of every *multi-mask*  $m \in \{1..N_m\}$  and for every MOD ( $X \in \{m, \sigma, S, K\}$ ) and every dataset ( $d \in \{Q, V, W, INC\}$ ) we define a parameter vector  $\mathbf{p} = \{r, m, d\}$  and independently calculate the tail probability  $P(X_{\mathbf{p},i})$  of occurrence of  $X_{\mathbf{p},i}$  value of the data in the  $N_{sim} = 10^4$  simulations, probing the corresponding probability distribution functions (PDF). The quantities  $m, \sigma, S, K$  correspond to the first four moments of distribution respectively. Hence we define  $P(X_{\mathbf{p},i})$  as:

$$P(X_{\mathbf{p},i}) \equiv P_q(|X_{\mathbf{p},i}^{sim} - Q_{2\mathbf{p},i}| > |X_{\mathbf{p},i}^{data} - Q_{2\mathbf{p},i}|) \quad (B1)$$

where  $Q_{2\mathbf{p},i}$  is the second quartile of the corresponding PDF, and  $P_q$  is the quantile tail probability.

In principle, considering  $N$  simulations allows us to probe a region of the underlying PDF corresponding to Gaussian number of "sigmas"

$$\pm n_\sigma^{MC} = \sqrt{2} \text{erf}^{-1}(1 - 2/N) = |\text{cdf}_G^{-1}(1/N)| \quad (B2)$$

where  $\text{cdf}_G^{-1}$  is the inverse Gaussian cumulative distribution function (CDF). For  $N = N_{sim} = 10^4$ , as it is the case for individual region statistics,  $n_\sigma^{MC} \approx 3.72$  corresponding to a probability of exceeding of 0.02%.

To derive the probability from Eq. B1, we use linearly interpolated quantile probability within the MC probed PDF range:

$$P(X_{\mathbf{p},i}) = \frac{Q_{lin}(X_{\mathbf{p},i})}{X_{\mathbf{p},i} \in (\min(X_{\mathbf{p},i}^{sim}), \max(X_{\mathbf{p},i}^{sim}))} \quad (B3)$$

where  $Q_{lin}$  is the linearly interpolated quantile probability, and  $\min(X_{\mathbf{p},i}^{sim})$  and  $\max(X_{\mathbf{p},i}^{sim})$  are the minimal and maximal  $X_{\mathbf{p},i}$  values obtained from a sample of  $N_{sim}$  simulations

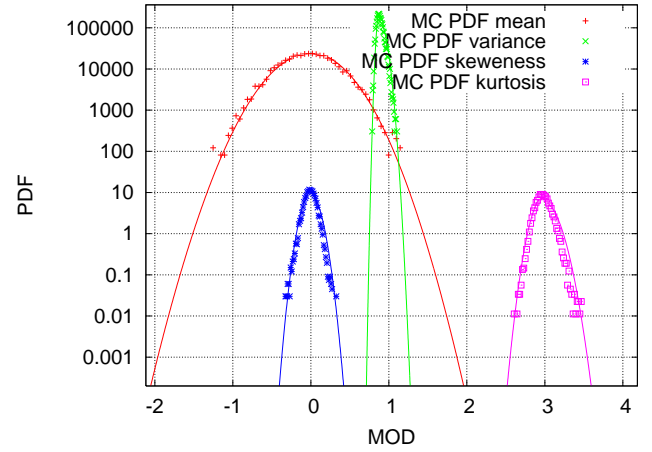


Fig 19: Example of extrapolation (solid lines) used to compute the distribution of  $10^4$  MODs from one of the regions in one of the *multi-masks*. Mean and variance MODs values were multiplied by a factor of  $10^4$  for the sake of clarity. Note that the Gaussian extrapolation (used only outside MC probed PDF region) also interpolates the data quite well in case of the means (red crosses).

that probe the underlying  $X_{\mathbf{p},i}$  PDF. Outside the probed range ( $X_{\mathbf{p},i} \in (-\infty, \min(X_{\mathbf{p},i}^{sim})) \cup [\max(X_{\mathbf{p},i}^{sim}), \infty)$ ) we extrapolate using a Gaussian distribution of the form

$$P(X_{\mathbf{p},i}) = \left(1 - \text{erf}\left(\frac{n_\sigma}{\sqrt{2}}\right)\right) n_\sigma = \begin{cases} n_\sigma^{MC} \left(1 + \frac{\min(X_{\mathbf{p},i}^{sim}) - X_{\mathbf{p},i}}{|\min(X_{\mathbf{p},i}^{sim}) - Q_{2\mathbf{p},i}|}\right) & ; X_{\mathbf{p},i} \leq \min(X_{\mathbf{p},i}^{sim}) \\ n_\sigma^{MC} \left(1 + \frac{X_{\mathbf{p},i} - \max(X_{\mathbf{p},i}^{sim})}{|\max(X_{\mathbf{p},i}^{sim}) - Q_{2\mathbf{p},i}|}\right) & ; X_{\mathbf{p},i} \geq \max(X_{\mathbf{p},i}^{sim}) \end{cases} \quad (B4)$$

Note that the extrapolation form is connected to the MC probed PDF range by the matching condition  $P(X_{\mathbf{p},i}(n_\sigma^{MC})) = P(\min(X_{\mathbf{p},i}^{sim})) = P(\max(X_{\mathbf{p},i}^{sim})) = 2/N$  - i.e. the probability of finding a  $X_{\mathbf{p},i}$  value anywhere in range  $(-\infty, \min(X_{\mathbf{p},i}^{sim})) \cup [\max(X_{\mathbf{p},i}^{sim}), \infty)$ . An example of this extrapolation is shown in Fig. 19. This extrapolation is obviously not validated for MODs higher than the mean, but we use it as a guide for very low probability events. Note that all our results with a lower significance (roughly outside  $3\sigma$  CL) are obtained modulo this approximation.

### 2. Multi-region joint analysis

In the multi-region analysis, we account for all correlations between regions of a given *multi-mask* using an unbiased estimator of the full covariance matrix. Using the same parameter vector  $\mathbf{p} = \{r, m, d\}$ , we define a one column vector for each MOD ( $\mathbf{X}_{\mathbf{p}} \in \{m_{\mathbf{p}}, \sigma_{\mathbf{p}}, S_{\mathbf{p}}, K_{\mathbf{p}}\}$ ) of size  $N_{reg}(r, m)$  such that  $\mathbf{X}_{\mathbf{p}} = (X_{r,m,d,i=1}, \dots, X_{r,m,d,i=N_{reg}(r,m)})^T$  contain  $X_{\mathbf{p},i}$  values for each region of a given *multi-mask*  $m$  of given pixelization scheme  $r$  and dataset  $d \in \{Q, V, W, INC\}$ . Introducing a parameter vector  $\mathbf{q} = \{X, r, m, d\}$  we define a corresponding  $\chi_q^2$  value as:

$$\chi_q^2 = (\mathbf{X}_{\mathbf{p}}^{data} - \langle \mathbf{X}_{\mathbf{p}}^{sim} \rangle)^T \mathbf{C}_q^{-1} (\mathbf{X}_{\mathbf{p}}^{data} - \langle \mathbf{X}_{\mathbf{p}}^{sim} \rangle) \quad (B5)$$

where the  $\langle \rangle$  is the average  $\mathbf{X}$  from  $N_{sim}(C_q)$  simulations and  $\mathbf{C}_q^{-1}$  is an unbiased estimator of the inverse covariance ma-

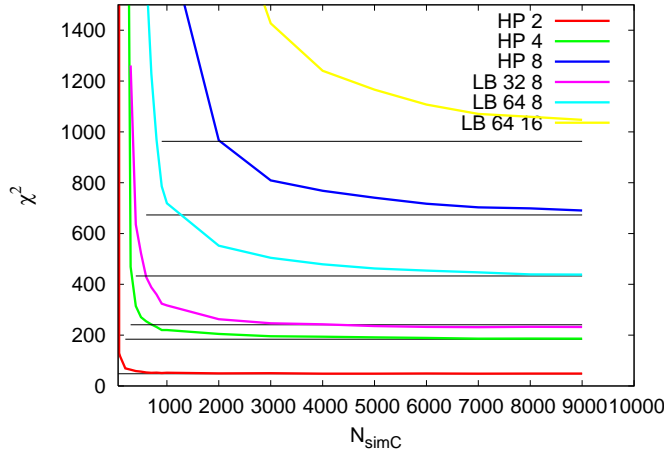


Fig 20: Convergence of  $\chi^2_q$  values as a function of the number of simulation used for the covariance matrix calculation for a given MOD. Each color corresponds to a type of pixelization schemes. The number of regions increases from bottom (48, for *HP 2*) to top (1024 for *LB 64 16*) (see. Table I). Horizontal lines indicate the effective numbers of degrees of freedom for that *multi-mask* (i.e. number of unmasked regions due to Kp03 sky mask). These  $\chi^2$  corresponds to the the first MOD only (mean) but other MODs exhibit similar dependence.

trix (Hartlap et al. 2007) calculated from  $N_{\text{sim}(C_q)}$  simulations and is given by:

$$(C_q^{-1})_{ii'} = \frac{N_{\text{sim}(C_q)} - N_{\text{reg}}(r, m) - 2}{N_{\text{sim}(C_q)} - 1} (\tilde{C}_q^{-1})_{ii'} \quad (\text{B6})$$

and  $\tilde{C}_p^{-1}$  is the inverse covariance matrix.

In Fig. 20 we show the convergence  $\chi^2_q$  with the number of simulations used to calculate the covariance matrix,  $N_{\text{sim}(C_q)}$ , for all six types of pixelization schemes. The biasing of the  $\chi^2_q$  values with regards to the ideal  $\chi^2_q(N_{\text{sim}(C_q)} = \infty)$  value is caused by the limited number of available simulations. As expected, for a given number of simulations, this bias decreases with the effective number of DOF and as such with the *multi-mask* resolution. We account for this biasing by using simulations to probe the underlying PDF of the  $\chi^2_q$  values, instead of using theoretical  $\chi^2$  distributions. In fact, it would not be valid to use theoretical  $\chi^2$  PDFs, since the distributions of individual MODs (except for the mean) are not Gaussian. As such, we will probe the underlying distributions using  $N_{\text{simPDF}(\chi^2_q)} = N_{\text{sim}} - N_{\text{sim}(C_q)}$  simulations, for each MOD and for each *multi-mask*.

In the case of the joint multi-region statistics we use  $N = N_{\text{simPDF}(\chi^2_q)} = 10^3$  simulations corresponding to  $n_\sigma^{\text{MC}} \approx 3.09$ , which gives a probability of exceeding and 0.2%. The remaining  $N_{\text{sim}(C_q)} = 9 \cdot 10^3$  simulations are used for covariance matrix calculation.

Given a  $(\chi^2_q)^{\text{data}}$  value we define a corresponding joint probability as:

$$P(\chi^2_q) \equiv 1 - P_q((\chi^2_q)^{\text{sim}} > (\chi^2_q)^{\text{data}}) \quad (\text{B7})$$

We use the same formulas for inter/extrapolation as described in Sect. B 1 by replacing  $X_{p,i}$  with  $\chi^2_q$ .

We note that, in fact, in case of the multi-region analysis it doesn't make any difference whether the derived  $\chi^2$  values are statistically debiased or not, since exactly the same biasing affects the simulated  $\chi^2$  values used to probe the underlying PDF. We also find that the convergence of such derived

Table VII: List of principal acronyms used in this section and in the main body of the paper, briefly summarized for quick reference. \* - indicates "unless specified otherwise".

Symbol	explanation
MOD	moment of distribution
data	upper index to indicate a measurement on data
sim	upper index to indicate a measurement on simulations
$N_m$	total number of <i>multi-masks</i> in a given pixelization scheme ( $N_m = 100^*$ )
$m$	<i>multi-mask</i> index number $m \in \{1, \dots, N_m\}$
$r$	pixelization scheme resolution parameter $r \in \{48, 192, 256, 512, 768, 1024\}$ (Tab. I)
X	MOD: $X \in \{m, \sigma, S, K\}$ , mean, variance, skewness, kurtosis respectively
$d$	dataset: $d \in \{Q, V, W, \text{INC}\}$
$N_{\text{reg}}(r, m)$	number of regions in $m$ 'th <i>multi-mask</i> of the pixelization scheme $r$
$i$	region index within a <i>multi-mask</i>
$\mathbf{p}$	parameter vector: $\mathbf{p} = \{r, m, d\}$
$\mathbf{q}$	parameter vector: $\mathbf{q} = \{X, r, m, d\}$
$X_{p,i}$	value of a MOD for $i$ 'th region of $m$ 'th <i>multi-mask</i> of $r$ 'th pixelization scheme in a dataset $d$
$N_{\text{sim}}$	total number of simulations;
$P(X_{p,i})$	number of simulations used in the single-region analysis probability corresponding to $X_{p,i}$ derived from $N_{\text{sim}}$ simulations (Eq. B1)
$n_\sigma^{\text{MC}}$	defined in Eq. B2
$\mathbf{X}_p$	vector of MOD values for for a given value of parameter $\mathbf{p}$
$N_{\text{sim}(C_q)}$	number of GRF simulations used to derive the covariance matrix in multi-region analysis ( $N_{\text{sim}(C_q)} = 9000^*$ )
$N_{\text{simPDF}(\chi^2_q)}$	number of GRF simulations used to probe the distribution of $\chi^2_q$ values in multi-region analysis ( $N_{\text{simPDF}(\chi^2_q)} = 1000^*$ )
$\chi^2_q$	$\chi^2$ value for the corresponding $\mathbf{X}_p^{\text{data}}$ (Eq. B5)
$P(\chi^2_q)$	probability corresponding to $\chi^2_q$ (Eq. B7)

probabilities is actually much better than one could infer when looking at the worst case of *LB 64 16* presented in Fig. 20. We estimate that the derived probabilities converge to their true values within  $\sim 10\%$  of that value in this worst case of *LB 64 16* pixelization scheme, while in case of the *HP 2* the convergence of the derived probabilities is  $\lesssim 2\%$ .

The statistical debiasing used for the  $\chi^2$  values matters however in our third-stage analysis, i.e. in case of the all-*multi-masks* analysis.

### 3. All Multi-masks analysis

There is no a unique way to generalize from the results of the multi-region analysis. Although the most straightforward way would be to compute the inverse covariance matrix between all the MODs and for all regions of all *multi-masks*, this turns out to be computationally not feasible.

Note the fact that the  $\chi^2_q$  values are partially correlated with each other, since they result from a different sampling of the same dataset. However the degree of correlation strongly depends on the particular *multi-mask* properties and resolutions. In particular the inter-*multi-mask* correlations are largest in the lowest resolution *multi-masks*. The smaller correlations between various *multi-masks*, the more additional information the *multi-mask* analysis explores about the dataset. Large inter-*multi-mask* correlations indicate that not much new information is gained making it unnecessary to process large number of *multi-masks*.

In the following, in order the integrate all the information probed by different *multi-masks* we calculate the cumulative

probability of rejecting the GRF hypothesis using the median distribution  $\overline{\varphi}(\chi_{\mathbf{q}_{\text{MC}}}^2)$  of all processed  $\chi_{\mathbf{q}_{\text{MC}}}^2$  distributions and the median  $\overline{\chi}_{\mathbf{q}}^2$  value of the data. Therefore we calculate the distribution and  $\chi_{\mathbf{q}}^2$  value as:

$$\begin{aligned}\overline{\varphi}(\chi_{\mathbf{q}_{\text{MC}}}^2) &= \langle \varphi(\chi_{\mathbf{q}_{\text{MC}}}^2/\text{DOF}_{\text{eff}}) \rangle_m \\ \overline{\chi}_{\mathbf{q}}^2 &= \langle \chi_{\mathbf{q}}^2/\text{DOF}_{\text{eff}} \rangle_m\end{aligned}\quad (\text{B8})$$

where  $\langle \rangle_m$  is the average over all *multi-masks*,  $\text{DOF}_{\text{eff}} = \text{DOF}(r, m)$  is the effective number of degrees of freedom which is a function of resolution  $r$ , of the pixelization scheme and of a particular *multi-mask* due to interplay with the sky cut.

We define the joint cumulative probability of rejecting the GRF hypothesis of the WMAP CMB data via inconsistency with our simulations as a function of  $\mathbf{q}$  analogically as in Eq. B7, and we use the same extrapolation and interpolation formula as in case of multi-region analysis.

### Appendix C: NOISE SIMULATIONS TESTS

Difference maps obtained from observations in nearly the same frequency, and with nearly the same beams profile provide a good opportunity to measure the statistical properties of the instrumental noise.

We have performed a reduced  $\chi^2$  tests, directly in pixel domain, of the difference maps obtained from different channels of the WMAP data (Q12, V12, QV and Q1V1) at the Healpix resolution  $n_s = 512$ , and compared with results of the same tests performed at a low Healpix resolution  $n_s = 4$ .

Since the covariance matrix of the noise realizations is well diagonal a single variate Gaussian statistics was assumed, and reduced  $\chi^2$  distributions used. The Q12 and V12 yielded a well consistency with the simulations at both resolutions. The QV and Q1V1 difference data however, turns out to be more troublesome. Whereas there is a good consistency at

high resolution, the low resolution reduced  $\chi^2$  tests show significant discrepancy yielding a ‘‘probability of rejecting’’  $P = 0.999963$  in case of QV map and  $P = 0.998$  in case of Q1V1 map. This result is also discussed in Sect. VE in light of the anomalous dipole component of the V band map.

We also performed a single-region, joint multi-region, and all *multi-masks* analyses on the Q12 difference map, using a subset of 10 selected *multi-masks* of the *HP 2* pixelization scheme. Since the low resolution analysis yields a quick convergence (Fig. 20 in Sect. B 2) a small number of 500 simulations were generated and half of them used for covariance matrix calculation, and the other half was used for probing distributions of the  $\chi^2$  values.

We found strong anomalies in the distribution of means (of which joint probability is well extrapolated using Eq. B4 outside the MC probed range (Fig. 19)). The variance of the scrambled  $\Delta$  maps show that the rms amplitude of the differences is limited to the  $1.7\mu\text{K}$  at these scales which is consistent with the limits to the residual systematical uncertainties in Q1 and Q2 channels of the WMAP (Hinshaw et al. 2003) at these scales. The constraint includes not only the systematical uncertainties but also possible differences due to uncorrelated white noise used in our simulations, which in principle in the regional statistics do not average out in the same way as the pre-whitened 1/f pink noise of the WMAP data.

A difference  $\Delta$  map of the variances can also serve as a rough estimate of the level of local systematical effects. Anomalies in the scrambled map are indeed found, with strongest deviations concentrated in parts of regions adjacent to the Galactic Center, with extreme values  $< 3\mu\text{K}$ . However a close orientation of the regions to the Galactic Center is more likely a hint on the residual foregrounds contamination, due to slight differences in the effective frequency of the Q1 and Q2 differential assemblies, as well as in the beam profiles, rather than a manifestation of a systematical effects. Due to this leakage the limits to the aforementioned systematical effects at the level of  $1.7\mu\text{K}$  should be considered as an upper limits.